ABSTRACT

Title of Document: PERFORMANCE MEASURMENT AND SIMULATION OF A SMALL INTERNAL COMBUSTION ENGINE

Nathan Lee Moulton
Master of Science, 2007

Directed By: Associate Professor Christopher Cadou
Department of Aerospace Engineering

This thesis describes performance testing of 3W Modellmotoren's 100i-B2 which is a two-stroke gasoline engine presently being used to power a commercially produced Unmanned Air Vehicle (NAVMAR's Mako). Since the engine was originally manufactured for use in radio controlled model aircraft, the only performance information provided by the manufacturer is its rated power output of 9.3 Hp at 8500 RPM. However, much more detailed information is required for the UAV application in order to select propellers and engine operating points that maximize the range, endurance, and load-carrying capacity. This thesis reports the first detailed characterization of this engine's performance in the open literature that includes measurements of power output, specific fuel consumption, exhaust and cylinder head temperatures, and exhaust gas composition as a function of engine speed. The measurements show that the peak power output is 9.32 Hp at 8500 RPM with a brake specific fuel consumption of 0.797 lb/Hp-hr. The maximum BSFC of

0.668 lb/Hp-hr is achieved during ¼ throttle operation at 6500 RPM with a power output level of 5.08 Hp. Exhaust gas composition measurements indicate that the carburetor controls mixture ratio effectively across the entire operating range of the engine unlike smaller model engines. A preliminary attempt was also made to simulate the engine numerically in order to identify areas where the engine design could be improved. The simulation suggests that while the engine's performance is near optimal, it might be possible to gain additional power by decreasing the exhaust port duration.

PERFORMANCE MEASUREMENT AND SIMULATION OF A SMALL INTERNAL COMBUSTION ENGINE

By

Nathan Lee Moulton

Thesis submitted to the Faculty of the Graduate School of the
University of Maryland, College Park, in partial fulfillment
of the requirements for the degree of
Master of Science
2007

Advisory Committee:
Associate Professor Christopher Cadou, Chair
Professor Norman Wereley
Associate Professor Kenneth Yu

Dedication

To my family and friends who have kept me going during this arduous task…I thank you.

To my parents…I cannot express how grateful I am for having this opportunity; I could not have done it without you. Your unconditional love and support has allowed me to accomplish something I never dreamed possible.

Acknowledgements

I would like to thank the United States Navy and the Minta Martin Foundation for supporting this work.

I would like to thank Jason Marcinkoski for designing the data acquisition and dynamometer control system as well as Andy Hart for helping to get the project going in the beginning. I would also like to thank Shyam Menon for developing the engine simulation program.

Finally and most importantly I would like to thank my mentor, Dr. Chris Cadou, for his guidance and continued support throughout my endeavor here at the University of Maryland.

Table of Contents

List of Tables

List of Figures

Chapter 1: Introduction

1.1 Background

Unmanned Air Vehicles (UAVs) are currently being utilized by the military for surveillance, reconnaissance, and combat missions. UAVs have been in military service since the 1940s where they originally served as target drones and primitive cruise missiles in World War II [1]. Their use as surveillance platforms began in the 1970's during the Vietnam War with the AQM-34 Firebee albeit in a limited role using pre-programmed flight paths for reconnaissance over North Vietnam and China [2]. The majority of missions involved taking still photographs and some included real-time video surveillance [3]. As technology has evolved, the size and weight of cameras and video equipment, avionics systems, communications equipment, etc. has decreased and awareness of the potential capabilities involving new roles and applications of UAVs is now being recognized [1].

The mainstream implementation of these aircraft for military applications is still in its infancy as most branches of the military have just begun flying UAVs within the past 10 years. As shown in Table 1.1, nearly all of the smaller UAVs (generally fewer than 2500 lb. gross weight) used for shorter range, low altitude missions are powered by reciprocating piston engines.

UAV	Gross Weight (lb)	Wingspan (ft)	Engine Make	Engine Type	Power/ Thrust	Fuel Type
Global Hawk	26,750	116.2	Rolls Royce AE-3007H	Turbofan	7,600 lb	JP-8
X-45A (J-UCAS)	12,189	33.8	Honeywell F124-GA-100	Turbofan	6,300 lb	JP
Fire Scout	3,150	27.5	Rolls Royce 250-C20W	Turboshaft	420 Hp	JP-5/JP-8
Eagle Eye	2,850	15.2	P&W 200-55	Turboshaft	641 Hp	JP/Diesel
Predator	2,250	48.7	Rotax 914 F	Reciprocating Piston	115 Hp	AVGAS
Hunter	1,620	29.2	Moto Guzzi (x2)	Reciprocating Piston	57 Hp (x2)	MOGAS
Snow Goose	1,400	6.8	Rotax 914 UL	Reciprocating Piston	110 Hp	MOGAS/ AVGAS
Pioneer	452	17	Sachs SF 350	Reciprocating Piston	26 Hp	AVGAS
Shadow	327	12.8	UEL AR-741	Rotary	38 Hp	MOGAS
Mako	130	12.8	3W 100	Reciprocating Piston	9.5 Hp	MOGAS

Table 1.1: Current and developmental UAVs [4]

Since the predominant mission of these vehicles is surveillance and reconnaissance, maximizing range and/or endurance is extremely important. The range of a fixed wing aircraft is given by the Brequet range equation [5]:

$$R = \eta_p \eta_{th} \frac{Q_R}{g} \frac{L}{D} \ln\left(\frac{m_i}{m_f}\right) \qquad \text{(Eq. 1.1)}$$

In this expression, Q_R is the energy density of the fuel, R is the range, η_p is the propulsive efficiency, η_{th} is the engine's thermodynamic efficiency, g is the acceleration due to gravity, L/D is the vehicle's lift to drag ratio, and m_i and m_f are the vehicle's initial and final masses. Eq. 1.1 shows that maximizing the product of the propulsive and thermal efficiency $\eta_p \eta_{th}$ maximizes the range of the aircraft. This is

accomplished by selecting the optimum propeller/engine combinations and operating points which, in turn, requires knowledge of the operating maps of the engine and propeller. Unfortunately, complete operating maps showing power, torque, and specific fuel consumption as a function of engine speed are usually not available for the engines used in these small UAVs. Usually, manufacturers only report peak power with the exception of one company [6]. Moreover, there is rarely any independent verification of the reported performance. Another important limitation is that most of these small engines consume gasoline instead of tactical fuels like DF2, JP4, or JP10. The United States military recognizes this fact and has listed as one of the main objectives on the Unmanned Aircraft Systems Roadmap for 2005-2030 by the Office of the Secretary of Defense is to "develop and field reliable propulsion alternatives to gasoline-powered internal combustion engines on UA 'Unmanned Aircraft', specifically their replacement with heavy fuel engines." Modifying current engines or designing new engines to consume tactical fuels like JP10 would simplify the logistic chain and increase vehicle range because the energy densities of these fuels is a factor of 13% greater than gasoline [7].

In order to improve upon engine performance, an understanding is needed of what the limits of present technology are. There have been some efforts to survey the current state of technology for small gasoline-fueled piston engines. In 1997, the Manchester Metropolitan University's Department of Chemistry performed a market analysis of the 2-stroke combustion engine industry [8]. Although the published data from the report is fairly limited, they did perform a review of the various application areas in which 2-stroke engines are used. One of them was remotely piloted military

aircraft where they listed that most small UAVs powered with 2-stroke gasoline engines have an engine displacement between 440-600 cm^3 and a power of roughly 50 kW/liter. Currently, the Department of Defense (DOD) has several unmanned vehicle programs utilizing small gasoline fueled engines. These include prominent vehicles like the Predator, Pioneer, and Hunter as well as some lesser known vehicles such as the Gnat, Hummingbird, Neptune, Mako, and Tern UAVs [4]. With the exception of the Predator vehicle which is powered by a Rotax engine, the performance maps for the rest of the engines being employed by this size class of UAVs are not published and most likely are not known.

1.2 Existing Work

There have been some efforts at the university level investigating small piston engines (generally under 100 Hp) in order to gain additional scientific understanding of the combustion process and engine design for the purpose of maximizing performance and efficiency while reducing emissions. The Engine Research Center (ERC) at the University of Wisconsin-Madison is currently conducting research involving optical diagnostic and imaging methods and computational fluid dynamics (CFD) [9, 10, 11, 12]. Their main focus is on spark ignition and diesel (compression ignition) engine analysis through the use of computer modeling and experimental tests. By combining the experimental data with the results of the numerical analysis through CFD, the ERC is seeking to improve the capabilities of the engine simulation analysis and apply it to real world applications. The center consists of eight engine test stations, each with an electrical dynamometer and control system. A picture of one such station is shown below.

Figure 1.1: Engine test station at ERC [13]

The ERC is currently testing and conducting research on a number of engines with full instrumentation and metering of various properties such as fuel and air flow rates and oil and water temperature and pressure. The engines include three large and two small single-cylinder diesel engines, five single-cylinder gasoline engines including 3 small engines, an optical gasoline engine, and a multi-cylinder diesel engine equipped with transient operation capabilities [13].

The Department of Mechanical Engineering at Kettering University recently tested a 500 cc. 2-stroke snowmobile engine manufactured by Yamaha operating on gasoline and on 10% and 85% ethanol-gasoline blends [14]. A Land & Sea water-brake dynamometer was used to measure torque and power while the engine's emissions were sampled by a Horiba MEXA 7100D exhaust gas analyzer. Although the main objective for their research was to determine the reduction in emissions and the consequences of using and storing ethanol, they published the power and torque

output from the engine while running at a 10% ethanol blend following the EPA 5-mode (Engine speed '% of max': 100, 85, 75, 65, idle) testing protocol for off-road engines. The published data for engine speed and torque as well as the calculated power corresponding to each data point is shown in Table 1.2. The results show that blending gasoline with ethanol reduced carbon monoxide production considerably over using gasoline only.

Mode	Engine Speed (RPM)	Brake Torque (Nm)	Calculated Power (kW)
1	7000	56.9	41.71071255
2	5950	29	18.06975632
3	5250	18.8	10.33604913
4	4550	10.8	5.146031911
5	idle	0	0

Table 1.2: Performance data for 5-mode EPA test [14]

At the University of Malaya, the Department of Engineering recently compared performance results from a 1.5 L gasoline engine that they retrofitted to run on compressed natural gas (CNG) with the stock performance [15]. An AG 150 (Froude Consine) eddy-current dynamometer was used for testing the car engine manufactured by Proton Magma. The testing was performed in two modes: in the first mode, the engine was held at a steady state condition at full or wide open throttle (WOT) while the speed was varied from 1500 to 5500 RPM, in the second mode, the speed was held constant at 2500, 3000, and 3500 RPM while the load was adjusted from 25 to 65% of max engine load. Engine performance including the brake mean effective pressure (BMEP), brake specific fuel consumption (BSFC), and emissions were measured and recorded. The results show that there was a 16% decrease in

BMEP in switching to CNG due to the longer ignition delay and lower flame speed, however the BSFC improved by decreasing on average of 18% due to the higher heating value of CNG and a leaner burning than that of the gasoline. The emissions were also improved by running CNG as all constituents but NOX decreased in value.

There has also been university research on smaller scale piston engines. This class of engines ('glow' fuel engines typically producing less than 1 to 2 Hp) has traditionally been reserved for the hobby enthusiast but has been gaining interest in the research community for commercial and military applications. At the University of Maryland, the research has focused primarily on performance measurements and possible scaling laws of these engines [16]. Of interest are their power output and efficiency and general performance trends as the engine size decreases. As shown in Figure 1.2, a custom dynamometer was designed and built to test the engines and acquire reliable performance data. Preliminary assessment of these engines is that they do not correspond to the performance data published by the manufacturers as the measurements obtained have been consistently lower than what is reported [17].

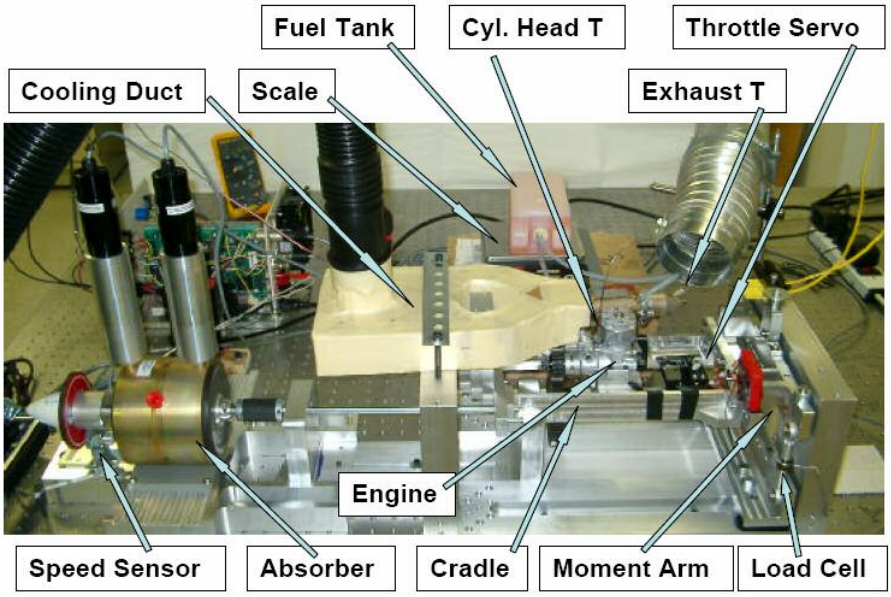

Figure 1.2: Dynamometer for measuring engine performance [16]

At the University of California, Irvine, current research is focused on developing portable power systems for autonomous technology [18]. Devices that require high power to weight ratios such as micro air vehicles and mobile robots will most likely require combustion supplied power. One possible solution is with small R.C. glow fuel engines. Similar to the dynamometer at the University of Maryland, a custom small engine dynamometer was constructed to measure the power and efficiency of these engines [19]. A schematic of the dynamometer is shown in Figure 1.3. Early results indicate poor efficiency performance and other techniques such as film combustion may be a solution.

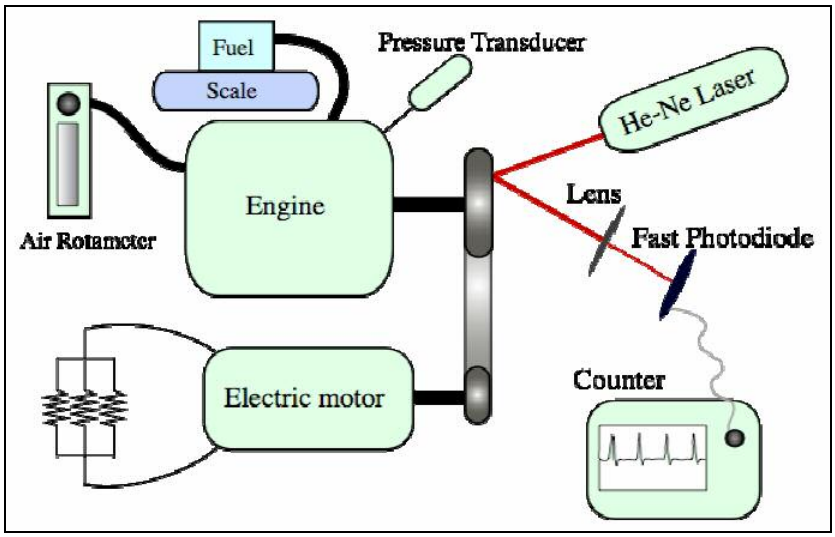

Figure 1.3: Small engine dynamometer schematic [18]

The University of California, Berkeley, is also researching portable power systems but has taken a different approach with the micro-size MEMS Rotary Engine Power System [20, 21]. As shown in Figure 1.4, they are constructing a hybrid power system consisting of an AC generator and a rotary internal combustion engine. The objective is to develop a power supply with a 5 to 15 percent increase in power output over existing battery technology. The development of the project is ongoing so the results are still pending.

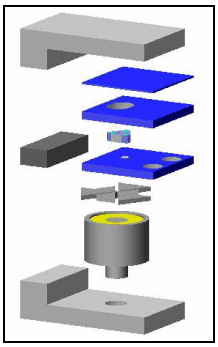

Figure 1.4: Model of MEMS Rotary Engine Power System [22]

Nevertheless, despite all of the active research at universities and institutions, the author is not aware of any research aside from the current paper that addresses a gasoline UAV piston engine of an intermediate size (approximately 10 to 20 Hp).

1.3 Approach

This thesis describes the complete characterization of the 100i-B2 engine manufactured by 3W Modellmotoren and currently used in two UAV programs by the military (NAVMAR's Mako and BAI Aerosystems' Tern UAVs). This engine was selected for testing because it is used in active systems and does not have a comprehensive performance database. The performance measurements reported include engine power, torque, specific fuel consumption, cylinder head and exhaust gas temperature, and exhaust gas composition – CO_2, CO, O_2, NO, NO_x, and unburned hydrocarbon concentrations. The development of the instrumentation, fixtures, and testing procedures are described. In addition, a numerical simulation of the engine developed by other researchers in our laboratory is used to make a zero-th order assessment of how the engine's performance would be affected by varying the intake and exhaust port timing and a few other simple design changes [23].

Chapter 2: Experimental Apparatus

2.1 Dynamometer System

An engine dynamometer was used to measure the performance of the 3W 100i-B2 engine. The apparatus consists of three main components: a custom built engine stand to mount the engine on, a water-cooled eddy current brake used to apply a load, and a data acquisition and control system for collecting data and controlling the engine and the brake. Figure 2.1 is a photograph of the dynamometer system with labels identifying the major parts. The engine to be tested is mounted on a movable support stand that consists of three plates; two side plates and a center plate upon which the engine is bolted to. This enables the dynamometer to accommodate a range of different sized UAV engines. The support stand slides along a grooved base plate to maintain alignment while providing various mounting locations for the different engine sizes. The engine drives the absorber through a 60 Hp rated Goodyear Eagle Pd belt drive system that serves as a 3:1 step down transmission. This is necessary because the maximum absorber operating speed is 4000 RPM whereas the maximum speed of the engine being tested, a 3W 100i-B2, is 8500 RPM. A Lovejoy SX90-6 flexible disc coupling between the engine and the transmission compensates for small amounts of angular, axial, and parallel misalignment between the engine's crankshaft and the transmission drive shaft. Two custom machined adapters are used to connect the crankshaft to the disc coupling while a combination of keys/keyways and set screws are used to hold the coupling in place.

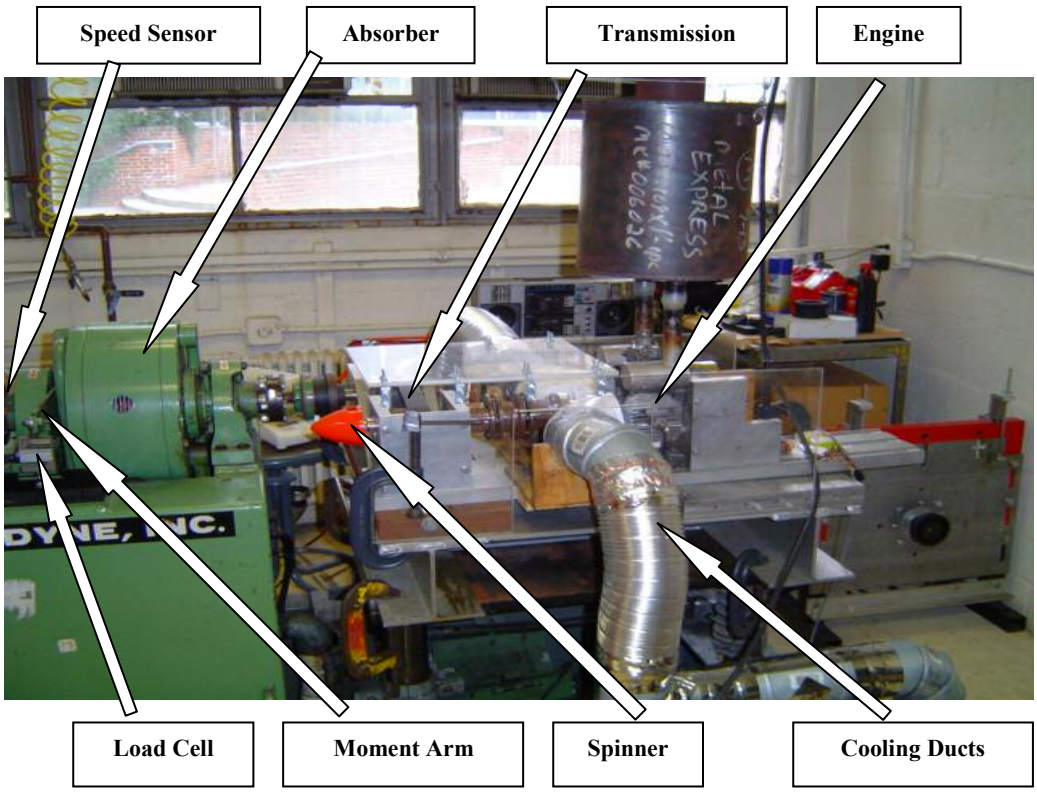

Figure 2.1: Photograph of dynamometer system and its major parts

Figure 2.2 is an assembly diagram of the engine support and transmission system illustrating the principal components. Belt tension is adjusted using a lead screw attached to a sliding carriage plate situated inside a larger stationary support plate. The carriage plate was machined of brass to minimize friction and subsequent abrasion between it and the larger steel stationary plate. The grooved base plate attaches directly to the carriage plate so that side loads associated with belt tensioning are not transferred to the engine crankshaft. The transmission sprockets are attached to their respective shafts using B-Loc B800 series shaft/hub locking devices. The drive shafts are each supported by two Koyo ball bearings, which are housed in pillow blocks, while retaining rings placed next to each bearing prevent the shafts

from sliding in the axial direction. An additional plate bolted between the two pillow blocks provides further reinforcement. A T.B. Woods Sure-Flex 6J flexible coupling between the output drive shaft and the absorber compensates for slight misalignments between the transmission and absorber.

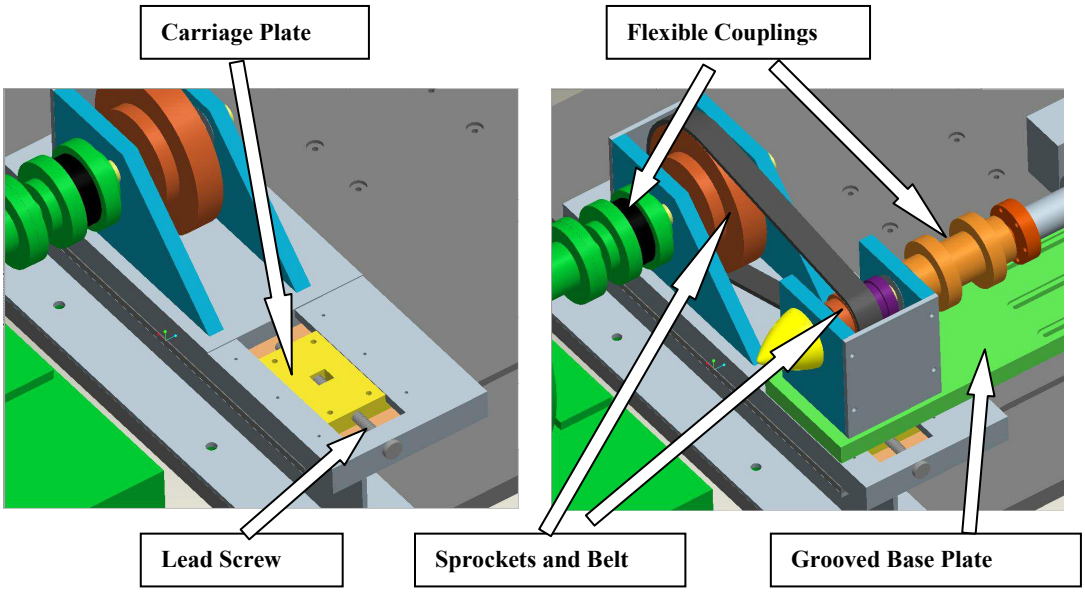

Figure 2.2: Diagram of transmission main components

The absorber is a water-cooled eddy current brake manufactured by Ostradyne Corporation with a maximum operating speed of 4000 RPM and a maximum power rating of 50 Hp. As shown in Figure 2.3, the absorber operates on the Foucault principle [24] which states that as a metallic mass (conductor) is traversed by an external magnetic field, an electro-magnetic force is induced. Electric currents known as eddy currents are produced in the conductor and in turn create a magnetic flux that opposes the external magnetic field. The stronger the magnetic field, the stronger the eddy currents developed and the larger the opposing magnetic force is.

In the case of the Ostradyne absorber, the conductor is the stator and the magnetic field is produced by exciting a coil located inside the stator. The strength of the magnetic field is varied by a rotor in the shape of a toothed wheel. As the teeth of the wheel cross the magnetic field, the strength of the field varies inducing eddy currents in the stator.

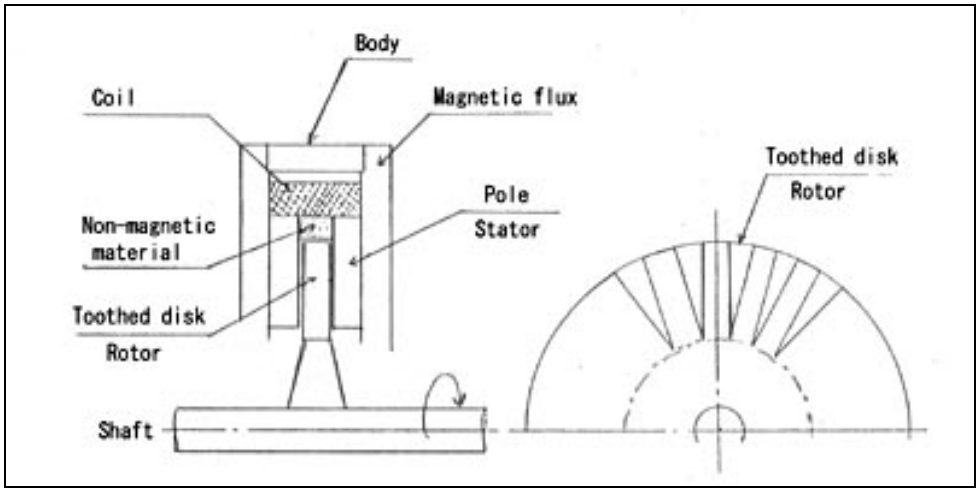

Figure 2.3: Diagram illustrating the main components of a typical eddy current brake [25]

The eddy currents convert the engine's power into heat so cooling water is circulated through cooling chambers around the stator so as not to overheat. The torque applied by the absorber is adjustable from zero to its maximum rated load by controlling the amount of current passing through the coil in the stator. The exciting current transmitted to the absorber is constant and completely independent of the engine speed; therefore the braking torque is also independent of speed. The amount of current supplied to the coil can be controlled using a manual control unit as shown in Figure 2.4, or an external analog signal. The latter approach is taken here in which

a computer running custom LabView software supplies the control signal. This allows the dynamometer to be operated in various modes which will be described later.

Figure 2.4: Control unit for exciting the eddy current dynamometer

The moment arm restraining force (and hence the engine torque) is measured using an Omega LCCA-100 S-beam load cell with a maximum capacity of 100 lb and 10 VDC excitation. The excitation voltage is provided by a 12 VDC power supply and a National Semiconductor LM2937 voltage regulator. A schematic of the electrical circuit is shown in Figure 2.5.

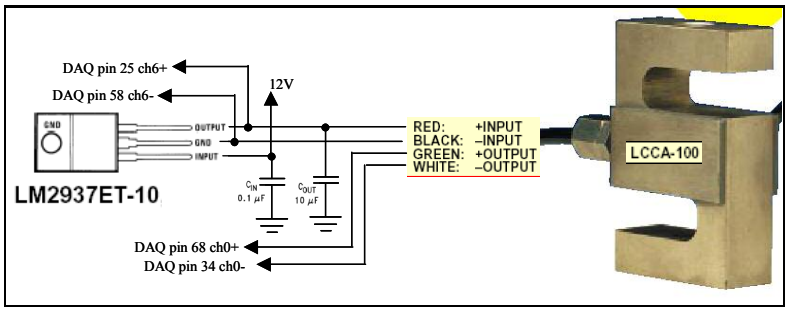

Figure 2.5: Load cell electrical circuit diagram [26]

As shown in Figure 2.6, the upper end of the load cell is attached to the absorber housing through a 9.25 inch long moment arm while the lower end of the load cell is connected to the dynamometer base. The load cell measures the force required to prevent the absorber housing (stator) from rotating and the product of this force and the moment arm length gives the torque applied to the engine.

Figure 2.6: Load cell attached to moment arm and dynamometer base

The speed sensor is a Fairchild Semiconductor H21B1 optical interrupter switch that uses an infrared emitting diode coupled with a silicon photodarlington detector. As seen in Figure 2.7, this sensor detects the passages of notches in a disk mounted to the absorber's output shaft. There are 12 notches on the disk so that one absorber shaft revolution corresponds to 12 pulses from the infrared emitting diode. The speed of the absorber shaft is the number of pulses per second divided by the

number of notches on the disk. The number of pulses per second is measured using a counter-timer channel on a National Instruments 6036E data acquisition board after the signal is buffered by a hex inverter. A circuit diagram is shown in Figure 2.8. The engine speed is the speed of the absorber shaft times the transmission step down ratio (3 in this case).

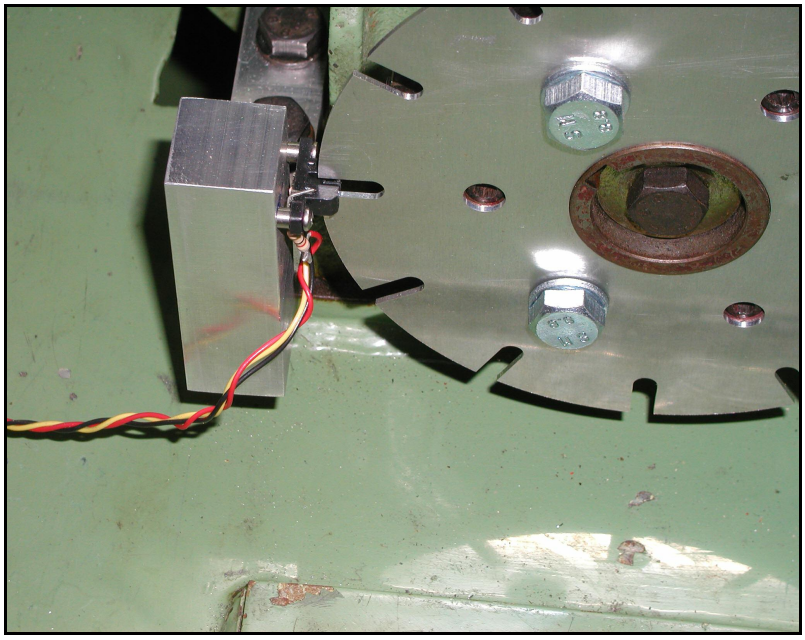

Figure 2.7: Speed sensor mounted next to notched disk

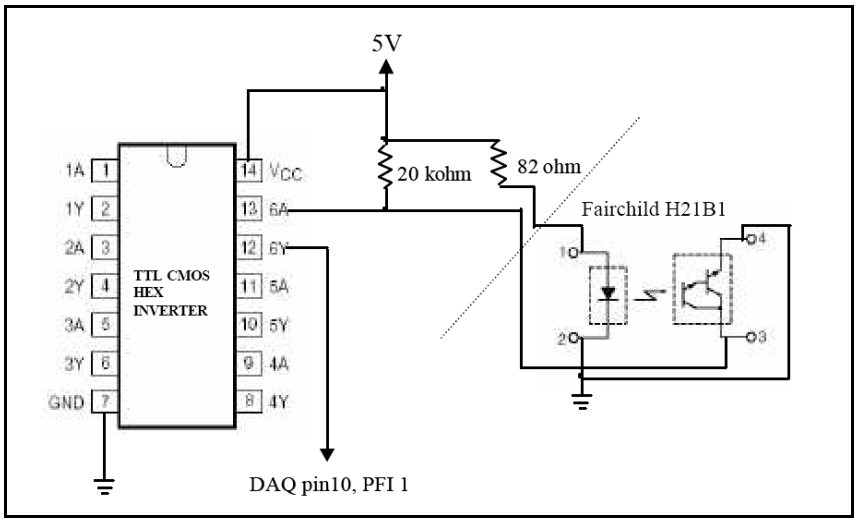

Figure 2.8: Speed sensor electrical circuit diagram [26]

K-type (Chromel Alumel) thermocouples are used for measuring cylinder head, exhaust gas, and auxiliary temperatures and are wired to an isothermal cold junction block. The junction block has copper terminals with copper wire connecting it to the data acquisition board. This, in effect, produces an additional thermocouple consisting of copper chromel and copper alumel. By connecting each wire on the isothermal junction block as shown in Figure 2.9 and measuring the temperature of the block, the additional voltage produced by the copper chromel and copper alumel thermocouple is accounted for.

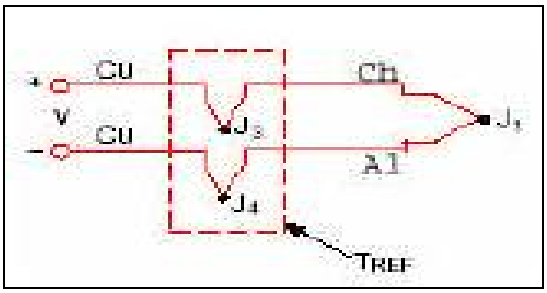

Figure 2.9: Isothermal junction block (represented by dotted line) [26]

Figure 2.10 shows the wiring diagram for the K-type thermocouples and associated connections on the junction block. A National Semiconductor LM35C temperature sensor is used to measure the temperature of the block and is also used for the ambient room temperature. Figure 2.11 displays the circuit diagram for the temperature sensor.

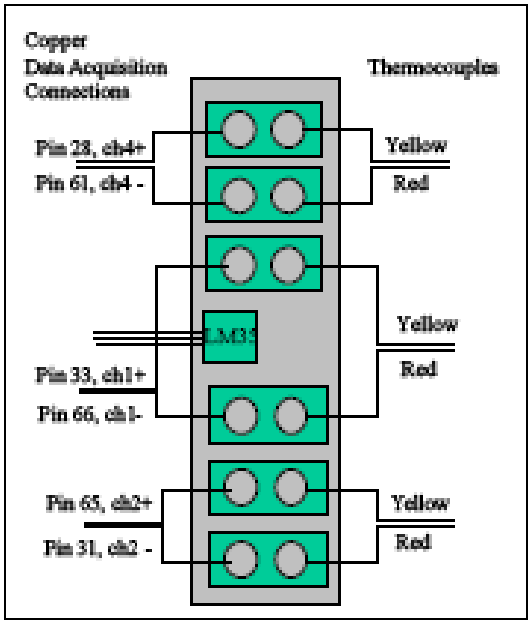

Figure 2.10: Thermocouple wiring diagram [26]

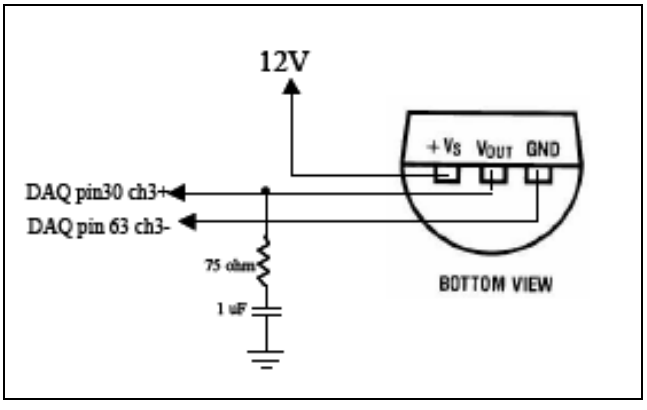

Figure 2.11: LM35C temperature sensor circuit diagram [26]

Figure 2.12 shows the custom graphical user interface (GUI) created using LabView software. The interface displays the engine's speed (RPM) on a tachometer, a streaming torque chart, calculated horsepower, throttle and load settings, amount of fuel left, thermocouple temperatures, and ambient room conditions among other items.

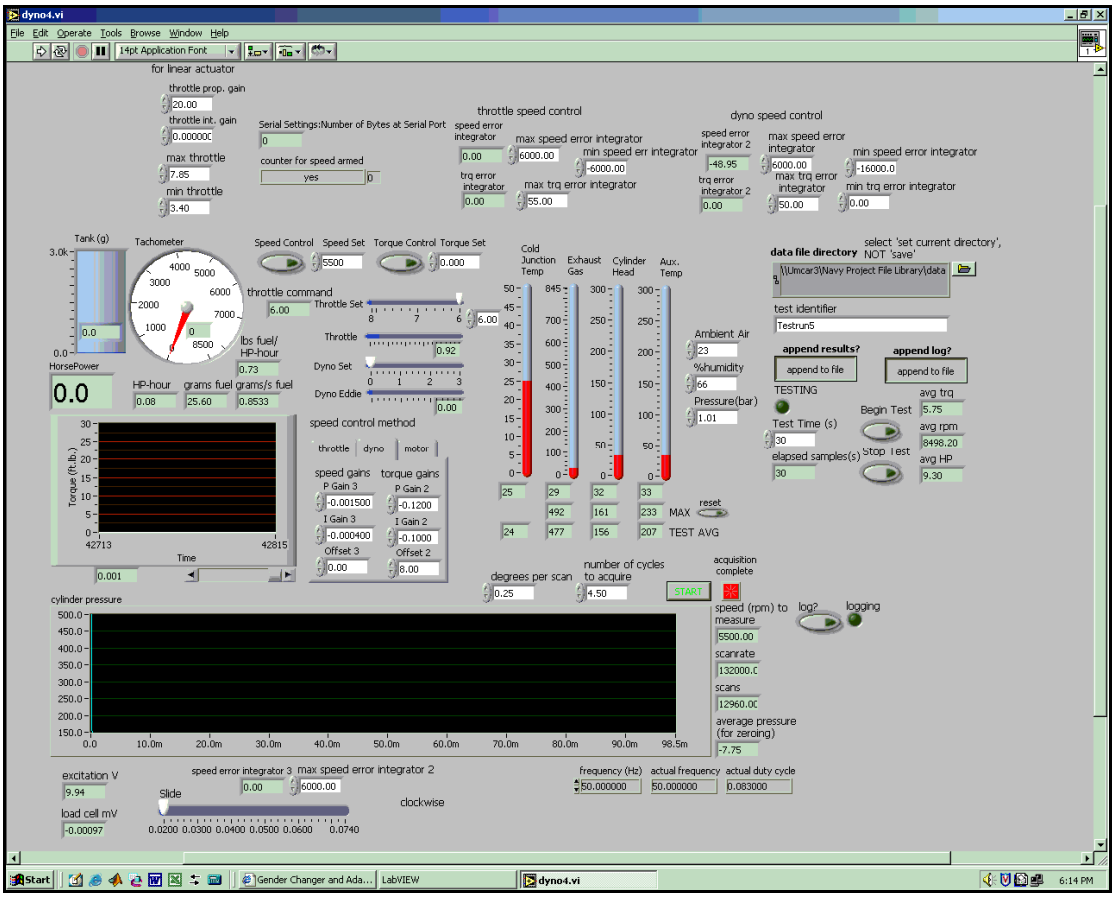

Figure 2.12: LabView custom graphical user interface (GUI)

The interface also allows the operator to control the engine's speed and torque by varying the throttle position and/or load applied by the eddy current absorber. This can be performed manually (open loop control) by manipulating the throttle set

and dyno set control sliders on the interface panel, or automatically (closed loop control) using a PI control scheme. Each PI scheme has two modes and each mode has two separate control techniques. The PI control uses a proportional (P) gain to decrease the response time and an integral (I) gain to eliminate the steady state error. The effect of changing these two parameters is seen in Table 2.1. The correct gains to use are found on an engine by engine basis since all engines have different operating characteristics. The tuning of these gains is done by trial and error usually starting with small gains and slowly increasing the values until the engine becomes unstable (i.e. speed oscillates, over speeds, stalls, etc.). When this happens, the gains have been set to high and will need to be lowered to return to stable operation.

Effects of changes in parameters				
Parameter	**Rise Time**	**Overshoot**	**Settling Time**	**S.S. Error**
P	Decrease	Increase	Small Change	Decrease
I	Decrease	Increase	Increase	Eliminate

Table 2.1: Performance effects of parameters [27]

These automatic modes facilitate the acquisition of constant torque and constant throttle setting performance curves. In the first mode (speed control), the throttle set slider is bypassed and the computer controls engine speed by varying the throttle while the operator controls the torque by varying the load using the dyno set slider. Alternatively, the dyno set slider can be bypassed so that the computer controls the speed by varying the load while the operator controls the torque by varying the throttle with the throttle set slider. In the second mode (torque control),

the throttle set slider is bypassed and the computer controls the torque by varying the throttle while the operator controls the engine speed by varying the load using the dyno set slider. Conversely, the dyno set slider can be bypassed so that the computer controls the torque by varying the load while the operator controls the speed by varying the throttle with the throttle set slider. An additional mode is also available but not used for the current testing. This mode is for motoring an engine, which is the process of turning the engine over or running it without fuel or spark ignition by means of a coupled electric motor. The mode controls the speed of the motor by varying the current sent to the motor's electric coils.

It should be noted that this particular engine is inherently unstable on the dynamometer because we are interested in operating points in the front half of the torque curve as shown in Figure 2.13. To understand why these points are unstable, consider what happens when the engine is running at a speed corresponding to Point A and there is a slight increase in speed. The engine's torque also increases as a function of speed and is now greater than the braking torque that is being applied. This causes the engine to accelerate toward Point B and it will continue increasing its speed unless the braking torque is increased to match the torque output of the engine. If the engine is at Point A and it experiences a slight decrease in speed, the engine's torque is now less than the torque being applied to it. This causes the engine to decelerate toward Point C and it will continue to decrease its speed until it stalls unless the braking torque is decreased to match the engine's torque. Therefore, the braking torque must be continuously adjusted so that the load being applied to the engine matches its torque output in order to maintain a constant speed. It is not

possible to make these adjustments manually and therefore the engine can only be operated on the dynamometer when the computer's speed control is turned on.

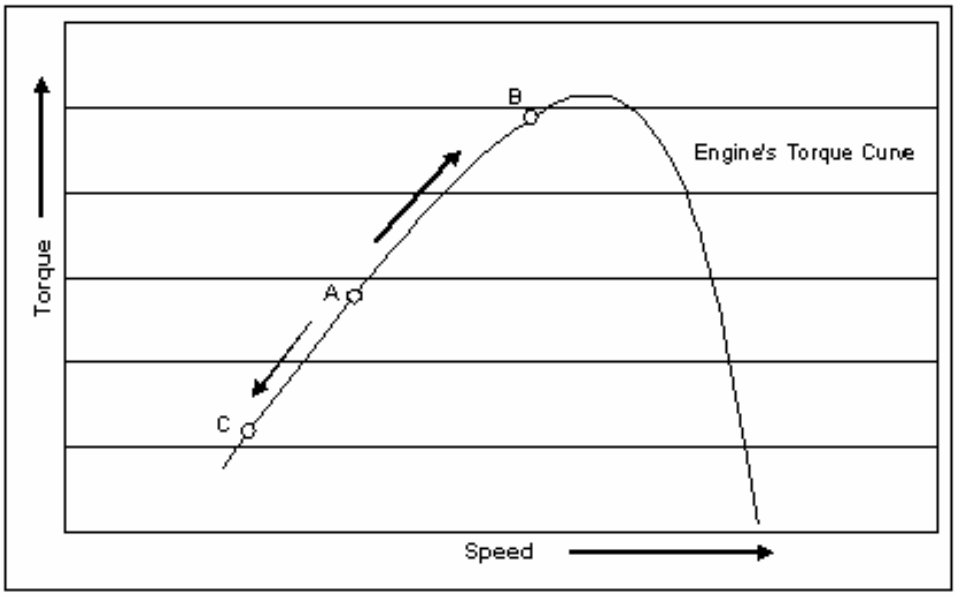

Figure 2.13: Engine's operating portion of torque curve

2.2 Engine Configuration

The engine, as can be seen in Figure 2.14, was tested as supplied by the manufacturer with a standard two-pipe exhaust system and no modifications of any kind. Table 2.2 lists the engine's technical specifications and operating characteristics. Procedures for engine break-in, startup, and leaning were followed as stated by the manufacturer in the engine operating manual. All measurements were performed using the factory specified mixture settings.

Figure 2.14: 3W 100i-B2 Engine [28]

Cylinder capacity	97.3 ccm / 5.83 cu.in
Power	6.8 kW / 9.3 HP
Bore dia.	44 mm / 1.73 in
Stroke	32 mm / 1.26 in
Speed range	1200 - 8500 min^{-1} / rpm
Weight	3190g / 7.0 lbs - incl. ignition
Crankshaft	3 Ball bearings
Connection rod	Needle bearings on both ends
Gasoline-Version	1 : 50 - 1 : 80 Mix
IIS – Ignition	4.8 V
Propeller	2-bladed: 24x10; 24x12; 26x10; 28x10; 30x8 3-bladed: 20x14; 22x11; 22x12; 24x10; 24x12; 26x10

Table 2.2: 3W 100i-B2 Engine Specifications [29]

2.3 Data Acquisition System

The data acquisition system also operates in the LabView environment and is integrated with the dynamometer control system. Analog signals from the torque sensor, speed sensor, and thermocouples are polled using the National Instruments 6036E data acquisition board. The accuracies for the analog inputs on the 6036E board are displayed in Table 2.3.

Nominal Range at Full Scale (V)	Absolute Accuracy							Relative Accuracy	
	% of Reading		Offset	Noise + Quantization (μV)		Temp Drift	Absolute Accuracy at Full Scale (mV)	Resolution (μV)	
	24 Hours	1 Year	(μV)	Single Pt.	Averaged	(%/°C)		Single Point	Averaged
±10	0.0546	0.0588	±1601	±933	±82.4	0.0010	7.56	1,085	108.5
±5	0.0146	0.0188	±811	±467	±41.2	0.0005	1.79	542	52.24
±0.5	0.0546	0.0588	±100	±56.2	±5.04	0.0010	0.399	66.3	6.630
±0.05	0.0546	0.0588	±28.9	±28.2	±2.75	0.0010	0.0611	36.2	3.616

Note: Accuracies are valid for measurements following an internal E Series calibration. Averaged numbers assume dithering and averaging of 100 single-channel readings. Measurement accuracies are listed for operational temperatures within ± 1 °C of internal calibration temperature and ±10 °C of external or factory calibration temperature. The Absolute Accuracy at Full Scale calculations use the maximum range input voltage (for example, 10 V on the ±10 V range) at one-year accuracy, assuming averaging.

Table 2.3: Accuracy information for the National Instruments 6036E data acquisition board [30]

Digital RS232 signals from the fuel scale are sent and received through the host PC's RS232 port using the LabView software. Data collection at a particular operating point is initiated by clicking a button on the user interface. The data is acquired at a frequency of 1 Hz. for a user-specified length of time (usually 2 1/2 minutes) and stored in the PC's memory until the test time has elapsed. Two files are then created and saved to the user specified directory. One file is a second by second log of all the data collected and the other file is a result file with averaged data values.

The keys for each file are presented in Table 2.4. Finally, the data acquisition board is also equipped with two analog output channels, which are used to generate the control signals for the absorber current and the throttle servo.

LOG FILE KEY
Each test begins with a line containing:
year,month,day,hour (24hr),minute of test
Followed by a line for every second of the test containing:
time (millisecond value)
fuel in tank (grams)
torque (ft-lb)
tachometer (RPM)
cylinder head temp (deg C)
exhaust gas temp (deg C)
cold junction temp (deg C)
auxiliary temp (deg C)
power (Hp)
load cell (mV)
load cell excitation voltage (V)

RESULT FILE KEY
Each line represents a test containing:
year,month,day,hour (24hr),minute of test
average torque over test (ft-lb)
average speed over test (RPM)
average power over test (Hp)
average fuel consumption over test (lbs fuel/Hp-hr)
fuel used in test (grams)
test length (s)
average load cell voltage (mV)
average load cell excitation voltage (V)
average head temp (deg C)
average exhaust temp (deg C)
average auxiliary temp (deg C)
average cold junction temp (deg C)
ambient air humidity (%)
ambient air pressure (bar)
ambient air temperature (deg C)

Table 2.4: Protocol for data files

2.4 Starting System

A plastic propeller spinner attached to the opposite end of the transmission input drive shaft allows the engine to be started using a standard model aircraft starter motor (Figure 2.15). The conical rubber adapter of the motor is pressed over the spinner to turn the engine. The starter motor is removed when the engine starts. The

engine throttle is actuated using a Hitec digital servo mounted behind the engine. The servo is controlled remotely through the LabView software program and an analog output on the National Instruments board. The board also provides the power for the servo so that no battery pack or receiver is needed.

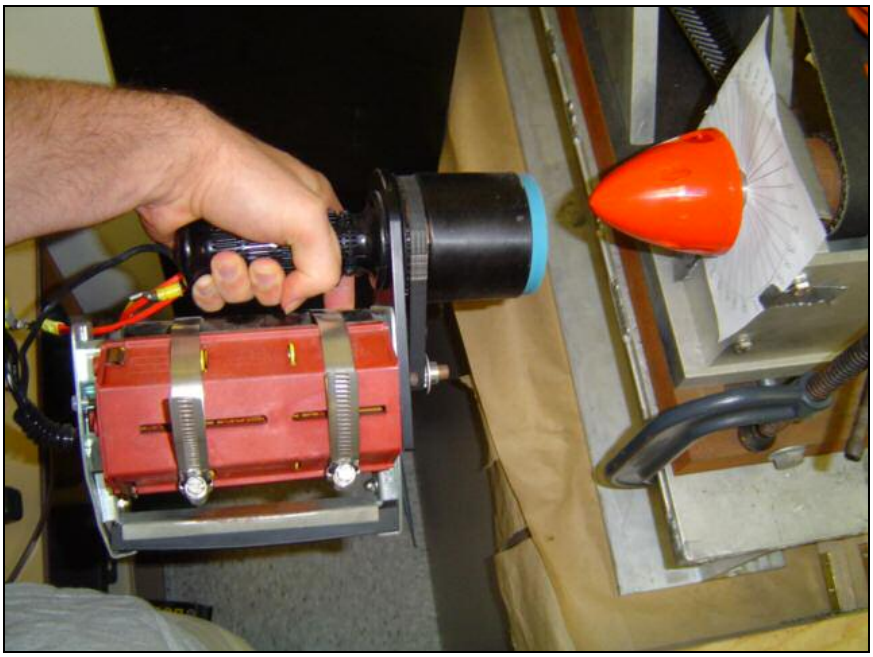

Figure 2.15: Starter motor and nose cone used to start engine

2.5 Fuel System

Fuel is supplied to the engine from a 1500 cc tank resting on an Acculab VIR-4800 portable scale equipped with an RS-232 output as shown in Figure 2.16. The data acquisition system polls the RS-232 output at 10Hz enabling the weight of the fuel tank to be measured as a function of time. The Du-Bro tygon fuel line runs from the tank to the fuel inlet located on the engine's carburetor. As seen in Figure 2.17, the carburetor is equipped with an integral diaphragm-type fuel pump that is driven

by the change in pressure between the crankcase and the environment through one engine cycle. As a result, no external fuel pump or pressurization of the fuel tank is necessary.

Figure 2.16: Fuel tank and scale with RS232 output

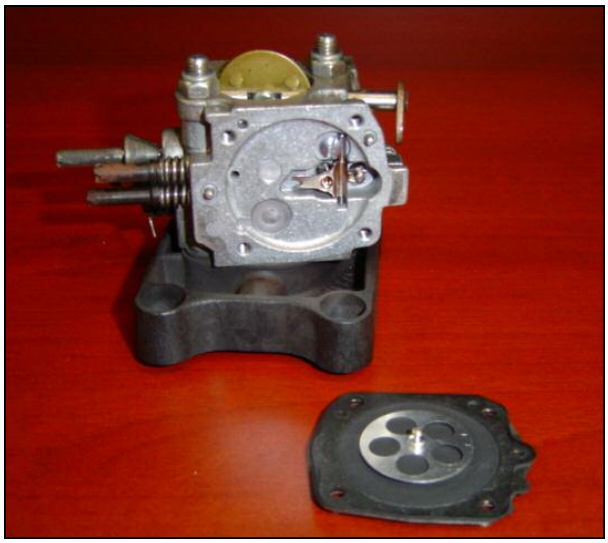

Figure 2.17: Carburetor with internal diaphragm fuel pump

2.6 Emissions Measurement System

The exhaust gas is sampled using a Vetronix PXA-1100 gas analyzer (Figure 2.18). The analyzer uses a non-dispersive infrared (NDIR) gas measurement bench and O_2 and NO_X sensors which measure the concentrations of five chemical species: CO, CO_2, O_2, NO_X, and total hydrocarbons (HC). It also calculates the air/fuel ratio based on the species concentration measurements for CO, CO_2, and O_2. As seen in Figure 2.19, the analyzer includes a sample hose that runs from the analyzer's intake port to a custom machined exhaust collector to measure the total exhaust output from both cylinders. The exhaust is sampled at a rate of 2Hz and the data is stored as a 'snapshot' on the analyzer. The data is then uploaded via an RS-232 output to the host PC using TechView software. The memory is limited on the gas analyzer and there is only enough room to hold five snapshots. Under the current configuration used for the testing, each snapshot represents a single test point. Therefore after acquiring five test points, the engine must be stopped so that the data can be uploaded to the computer. This clears the analyzer's memory so that it is capable of storing additional snapshots.

Figure 2.18: Exhaust gas analyzer with LCD display

Figure 2.19: Custom machined exhaust plenum

2.7 Cooling System

The cooling air for the engine is normally supplied by the propeller's wash and the relative motion of the UAV through the air. Since the engine is under stationary conditions on the ground, a cooling system was designed to prevent the engine from overheating. It consists of two sets of three blowers (Toro Electric Super Blower Vac, Model 51591) mounted on either side of the test platform that deliver air across each cylinder via two manifold/duct systems - one for each cylinder. A photograph of one set of blowers with its duct system is presented in Figure 2.20.

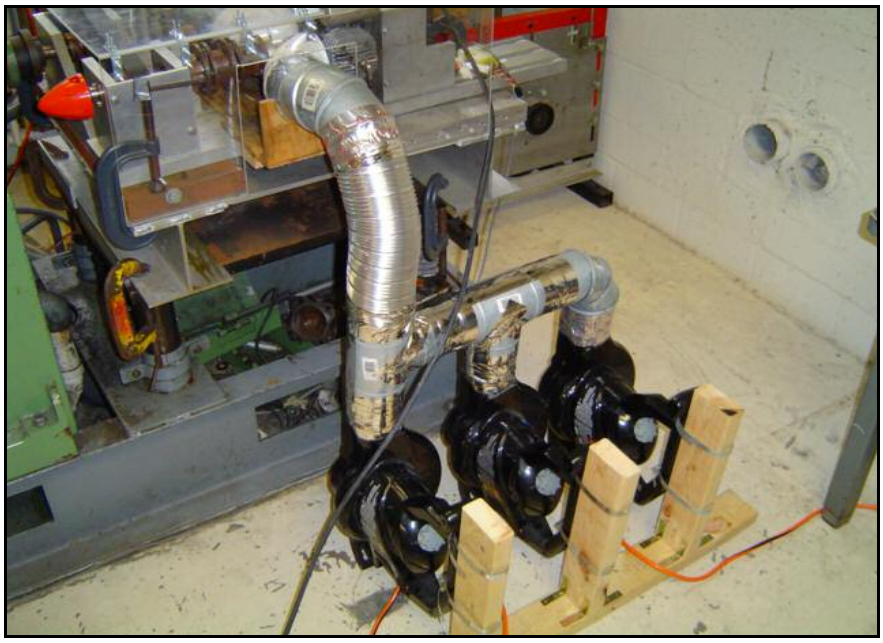

Figure 2.20: Photograph of blowers and duct system

Surface-mount K-type thermocouples (Omega CO3-K) attached to each cylinder between the cooling fins monitor the cylinder head temperature. Additional thermocouples are attached inside the muffler to monitor the exhaust gas temperature.

Figure 2.21 shows the attachment points of the cylinder head and exhaust manifold thermocouples. Each thermocouple is connected to an isothermal junction block, where a National Semiconductor LM35C temperature sensor is used to compensate for the cold junction block and obtain ambient air temperature. All thermocouples are polled by the LabView software.

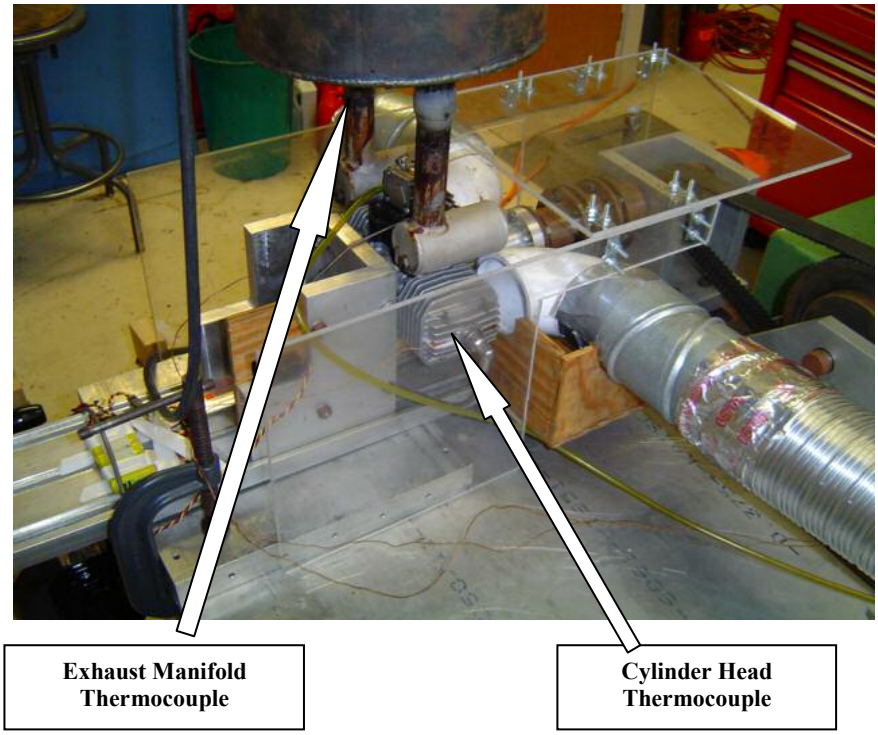

Figure 2.21: Photograph of thermocouple attachment points

Chapter 3: Experimental Procedure

3.1 Preparation

A check-list is used to prepare for each experiment. The list starts with charging the batteries for both the engine starter and the ignition system the night before as they require eight and fifteen hours, respectively, for a full charge. On the day of the test, each experiment begins by following the prescribed steps:

1. Turn on the exhaust gas analyzer. This is done first because the internal, infrared gas detectors and sample chamber need to warm up before the analyzer can be used. The process takes approximately fifteen minutes to complete the warm up cycle and the user can focus on other tasks while it is initializing itself. After the warm up is complete, the gas analyzer's measurement bench (HC, CO, CO_2), O_2 and NO_X sensors, and sample hose must be purged with fresh air in order to remove any residual hydrocarbons and moisture that can foul the measurement reading. Then the gas analyzer is zeroed so that the measurement bench and sensors read zero relative to the ambient air. The analyzer must also be purged and zeroed after using it for an extended period of time and notifies the user by displaying a message on the LCD screen when the action is needed. The particular length of elapsed time depends on various factors such as the type of engine, the engine speed, and the throttle setting among other items. For this specific engine experiment the

analyzer usually required a purge and zero about every ten to fifteen minutes of continuous testing and was generally done in between collecting data sets.

2. Prepare a fresh mixture of fuel consisting of a 50:1 ratio of regular unleaded gasoline and synthetic two-stroke oil (Homelite Exact Mix was used for this experiment). The fuel tank is filled through the breather tube and the fuel line is then connected to the carburetor. After the scale is zeroed, the fuel tank is placed on it.
3. Check the calibration of the throttle servo to make sure that the throttle (butterfly valve) is able to fully open and close so that the engine can go from an idle up to WOT.
4. Check the cooling system to make sure the blowers have electric power and that the manifold/duct system's connections are tight and are not leaking any air.
5. Check the propeller cone to make sure it is bolted securely to the end of the driveshaft.
6. Check the tension of the transmission belt using a belt tension gauge. A Goodyear Small Industrial Eagle Pd Gauge, shown in Figure 3.1, is used to measure the tension by first placing a straight edge across the top of the belt so that it extends the entire span of the belt from one sprocket to the other. Next, the gauge is placed in the center of the belt and at the middle of the belt span between the sprockets. A force is then applied to the gauge until the belt deflection, relative to the straight edge, corresponds to a predetermined value on the gauge's scale. If the measured force equals the target deflection force

then the belt is properly tensioned, if the force does not equal the target value then the tension is either increased or decreased to provide the desired deflection force. Figure 3.2 is a diagram of the tensioning procedure.

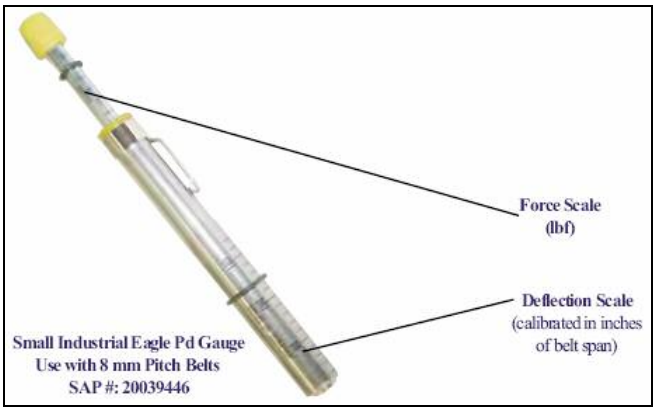

Figure 3.1: Belt gauge used for tensioning [31]

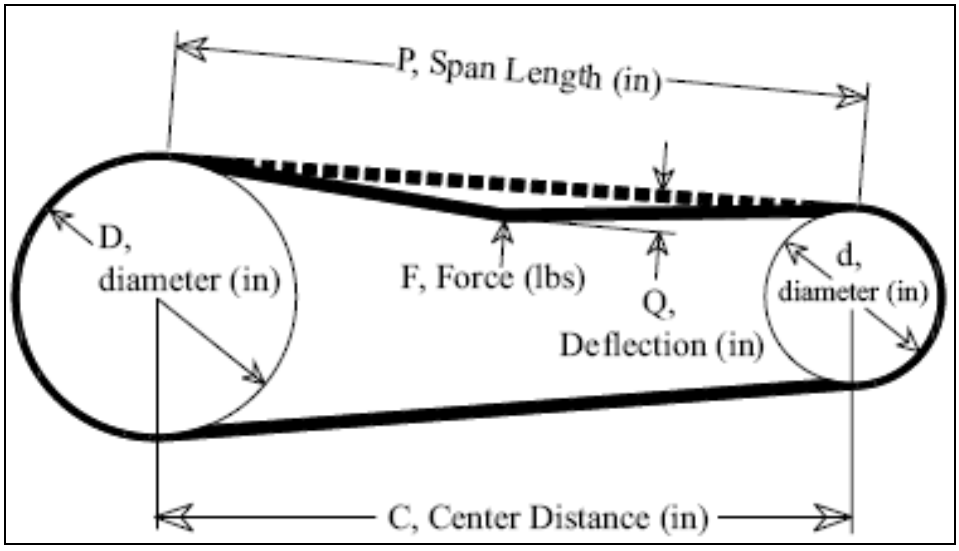

Figure 3.2: Tensioning diagram [31]

7. Check all sensors and wires for secure attachment and proper clearance from moving parts, hot surfaces, etc. These include the fuel tank's output cable, the cylinder head and exhaust gas thermocouples, the exhaust gas analyzer probe, the speed sensor, and the load cell.
8. Attach the ignition wires to the spark plugs, connect the ignition box to the engine's magnetic sensor, and then turn the ignition on.
9. Turn on the power supply and cooling water for the dynamometer's absorber and the exhaust fan and cooling blowers for the engine.
10. Start the LabView program and record the ambient conditions (i.e. room temperature, barometric pressure, and relative humidity). The load cell used for the torque measurements is zeroed by the LabView program each time it is started so that background interference is not measured. Sources of interference include cooling water running through the absorber, airflow from the exhaust fan and cooling blowers, and vibrations from the blowers.

3.2 Operation

After completion of the preparation check list, the engine is started and the LabView speed controller is set to a predetermined value (generally 4000 RPM) for the purpose of warming up the engine. Each test point is measured at a set speed with a fixed throttle position. In this manner, a test matrix is compiled and constant throttle setting performance curves are able to be obtained. A typical test begins with the engine being brought up to WOT and the speed set to the engine's maximum of 8500 RPM. Once the engine's torque, temperature, exhaust emissions, and other properties have stabilized, data is acquired for 150 seconds by the LabView system at

1 Hz. and the Vetronix gas analyzer at 2 Hz. The engine's speed is then set to subsequent test points at 1000 RPM decrements in order to cover the available operating RPM range for that particular throttle setting (i.e. 8500, 7500, 6500, etc.) At each test point, the engine requires approximately 1 to 2 minutes to stabilize before data is collected. The throttle position is then changed and the RPM range is swept again in a similar fashion. The testing repeats itself for the following throttle settings: WOT, ¾, ½, and ¼ throttle. The testing is concluded after each throttle setting has spanned its available operating RPM range.

3.3 Data Analysis

The data acquired from each sensor is stored in two files. The "log" file contains the raw data acquired each time the LabView software polls the sensors and the "result" file that contains the time averaged values for each test point. The data from the result file is averaged with data collected in other identical tests to calculate an overall average.

The principal engine performance measurements [32] are torque, power output, and efficiency. The torque produced by the engine is given by:

$$\Gamma = F \times d \qquad \text{(Eq. 3.1)}$$

Where F is the force measured by the load cell and d is the length of the moment arm (9.25 in). The power output is given by:

$$P = \Gamma \times \omega \qquad \text{(Eq. 3.2)}$$

Where Γ is the engine torque and ω is the angular speed of the output shaft. The overall efficiency of the engine is:

$$\eta = \frac{P}{\dot{m}_f Q} \tag{Eq. 3.3}$$

Where P is the power output, $\dot{m}_f$ is the fuel mass flow rate, and Q is the energy density of the fuel (44.5 MJ/kg) [33]. Alternatively, the efficiency can also be reported in terms of the brake specific fuel consumption (BSFC).

$$BSFC = \frac{\dot{m}_f}{P} \tag{Eq. 3.4}$$

Other measurements include cylinder head and exhaust gas temperature and exhaust gas composition. The latter consists of measurements of CO, CO_2, O_2, NO_X, and total hydrocarbons (HC). Air/fuel ratio is computed from the exhaust gas composition measurements by solving a chemical equilibrium balance. The general hydrocarbon combustion reaction per mole of fuel is defined as follows [33].

$$\begin{aligned} &C_{\alpha+}H_\beta O_\gamma N_\delta + \frac{a_s}{\phi}\left(O_2 + 3.76N_2\right) \rightarrow n_1 CO_2 + n_2 H_2 O + n_3 N_2 + \\ &n_4 O_2 + n_5 CO + n_6 H_2 + n_7 H + n_8 O + n_9 OH + n_{10} NO + n_{11} N + \\ &n_{12} C(s) + n_{13} NO_2 + n_{14} CH_4 + \ldots \end{aligned} \tag{Eq. 3.5}$$

For the combustion reaction in a gasoline engine, ignoring negligible products, the equilibrium balance can be approximated as:

$$\begin{aligned} &C_{\alpha+}H_\beta O_\gamma N_\delta + \frac{a_s}{\phi}\left(O_2 + 3.76N_2\right) \rightarrow n_1 CO_2 + n_2 H_2 O + \\ &n_3 N_2 + n_4 O_2 + n_5 CO + n_6 H_2 + n_7 CH_z(g) \end{aligned} \tag{Eq. 3.6}$$

Where:

$$z = \beta / \alpha \tag{Eq. 3.7}$$

Performing a carbon-oxygen balance and solving for the equivalence ratio, yields the following expression:

$$\phi = \frac{2\left(1 + \frac{1}{4}\frac{\beta}{\alpha} - \frac{1}{2}\frac{\gamma}{\alpha}\right)(y_1 + y_5 + y_7)}{2y_1 + y_2 + 2y_4 + y_5} \qquad \text{(Eq. 3.8)}$$

Where α, β, and γ represent the number of carbon, hydrogen, and oxygen atoms present in the unburned fuel (for gasoline α=7, β=17, γ=0) [33], and y_i denotes concentrations of the various product constituents in mole percent. Knowing the equivalence ratio and that the stoichiometric air/fuel ratio for gasoline is 14.7 [34], the actual air/fuel ratio is then solved for.

$$A/F = \frac{14.7}{\phi} \qquad \text{(Eq. 3.9)}$$

3.4 Performance Correction

Since engine performance varies with atmospheric conditions, the WOT data for power output must be corrected to a reference or standard condition so that measurements made on different days may be compared. The formula for corrected engine power is [35]:

$$bp_c = CA \times bp_o \qquad \text{(Eq. 3.10)}$$

Where bp_c is the corrected brake power, CA is the atmospheric correction factor, and bp_o is the observed brake power. Since friction power (the power required to drive the engine without combustion) is unknown, an 85% mechanical efficiency is assumed [35]. Using this assumption, the calculation of the atmospheric correction factor is:

$$CA = 1.18\left[\left(\frac{99}{P_d}\right)\left(\frac{T_o + 273}{298}\right)^{0.5}\right] - 0.18 \qquad \text{(Eq. 3.11)}$$

Where P_d is the dry air portion of the observed total inlet air supply pressure and T_o is the observed inlet air supply temperature. P_d is determined from the saturation vapor pressure (E_s), the relative humidity (RH), and the total barometric pressure (P_{tot}). The saturation vapor pressure is given by [36]:

$$E_s = c_0 \times 10^{\left(\frac{c_1 \times t_o}{c_2 + t_o}\right)} \quad \text{(Eq. 3.12)}$$

Where c_0, c_1, and c_2 are constants equal to 6.1078, 7.5, and 237.3 respectively. The actual vapor pressure (P_v) is calculated using the relative humidity.

$$P_v = RH \times E_s \quad \text{(Eq. 3.13)}$$

Finally, it is possible to calculate the dry air pressure:

$$P_d = P_{tot} - P_v \quad \text{(Eq. 3.14)}$$

3.5 Uncertainty Analysis

An uncertainty factor also needs to be placed on the data, due to the systematic and random errors present in the experiment. Standard procedures [37] are used to determine the 95% confidence interval for the measurements. The uncertainty for a particular measurement is:

$$\delta M = 2\sqrt{\left(\frac{B}{2}\right)^2 + \left(S_{\bar{x}}\right)^2} \quad \text{(Eq. 3.15)}$$

Where B is the total systematic error in the measurement and $S_{\bar{x}}$ is the random error present. The total systematic error (B) is found using:

$$B = \left[\sum_{i=1}^{K} b_i^2\right]^{1/2} \quad \text{(Eq. 3.16)}$$

Where b_i is each elemental systematic error and K is the total number of systematic error sources. The random error is given by:

$$S_{\bar{x}} = \frac{1}{\sqrt{N}}\left[\frac{1}{N_p - 1}\sum_{k=1}^{Np}\left(X_{p_k} - \overline{X}_p\right)^2\right]^{1/2} \qquad \text{(Eq. 3.17)}$$

Where N is the number of measurements, N_p and X_p are the previous measurement number and measurement value recorded by the instrument during the experiment, and $\overline{X}_p$ is given by:

$$\overline{X}_p = \frac{1}{N_p}\sum_{k=1}^{N_p} X_{p_k} \qquad \text{(Eq. 3.18)}$$

The uncertainty in a result (like power output) which is calculated from several measured quantities is found by:

$$\delta R = \sqrt{\left(\theta_1 \delta M_1\right)^2 + \cdots + \left(\theta_k \delta M_k\right)^2} \qquad \text{(Eq. 3.19)}$$

Where δM_κ is the uncertainty in each measurement and θ_κ is the sensitivity coefficient of the result to changes in the particular measured quantity. Table 3.1 lists systematic uncertainties for the major components of the dynamometer system.

Instrument	Function	Uncertainty	Units
NI 6036E data acquisition board	Acquire and log data	0.00756	volts
Omega LCCA-100 S-beam load cell	Measure engine torque	0.165	newtons
Fairchild H21B1 optical interrupter switch	Measure engine speed	0.0001	seconds
Acculab VIR-4800 scale	Measure fuel consumption	0.1	grams
Omega CO3 K-type thermocouple	Measure engine temperatures	1.8	degrees C
Vetronix PXA-1100 gas analyzer	Measure exhaust concentrations	5	% of reading

Table 3.1: Measuring instruments and uncertainties

Chapter 4: Experimental Results

4.1 Discussion

Figure 4.1 shows engine torque, power, fuel/air ratio, and efficiency as a function of engine speed at four throttle settings: WOT, ¾, ½, and ¼ throttle. The results represent averages computed using data from 19 separate test runs. The data show that the engine produces its rated power output of 9.3 Hp [29] at its maximum operating speed of 8500 RPM at WOT. At this operating point, the overall efficiency is 14.0% (BSFC = 0.797 lb/Hp-hr), and the air/fuel ratio is 15.38. The 'best economy' operating point occurs at 6500 RPM and WOT where the power output is 7.7 Hp, the overall efficiency is 16.1% (BSFC = 0.695 lb/Hp-hr), and the fuel/air ratio is 16.59. All of the data used to generate Figures 4.1 and 4.2 are presented in Tables 4.1 and 4.2.

The engine's torque curve is similar in shape to those of much larger engines. It increases non-linearly with speed until reaching a peak value after which it starts declining. However, at all throttle positions the data show a small decrease in torque at 5500 RPM that cannot be attributed to experimental uncertainty alone.

The air/fuel ratio data show that decreasing the throttle setting (i.e. closing the throttle) decreases the air/fuel ratio at operating speeds above 4000 RPM. This occurs because closing the throttle obstructs the flow of air into the engine (thereby decreasing the air flow rate) but does not affect the fuel flow rate that is set by (and increases linearly with) the operating speed of the engine. There is not a substantial

increase in power output between ¾ and WOT because the air/fuel ratio is greater than 14.7, the value for stoichiometric combustion of gasoline with air. Closing the throttle below ¾ lowers the air/fuel ratio below that required for complete combustion and the engine loses power because there is not enough oxygen to react with all the fuel.

At engine speeds below 4000 RPM, the throttle becomes less effective because the flow rate and pumping losses are lower. This allows the engine to ingest air more easily and the air/fuel ratio increases well above the stoichiometric value. The burning rate of the mixture peaks at the stoichiometric air/fuel ratio but decreases non-linearly with increases or decreases in air/fuel ratio. As a result, it is not possible to operate the engine at low speeds and high throttle settings because the burning rate of the high air/fuel ratio mixture is too low.

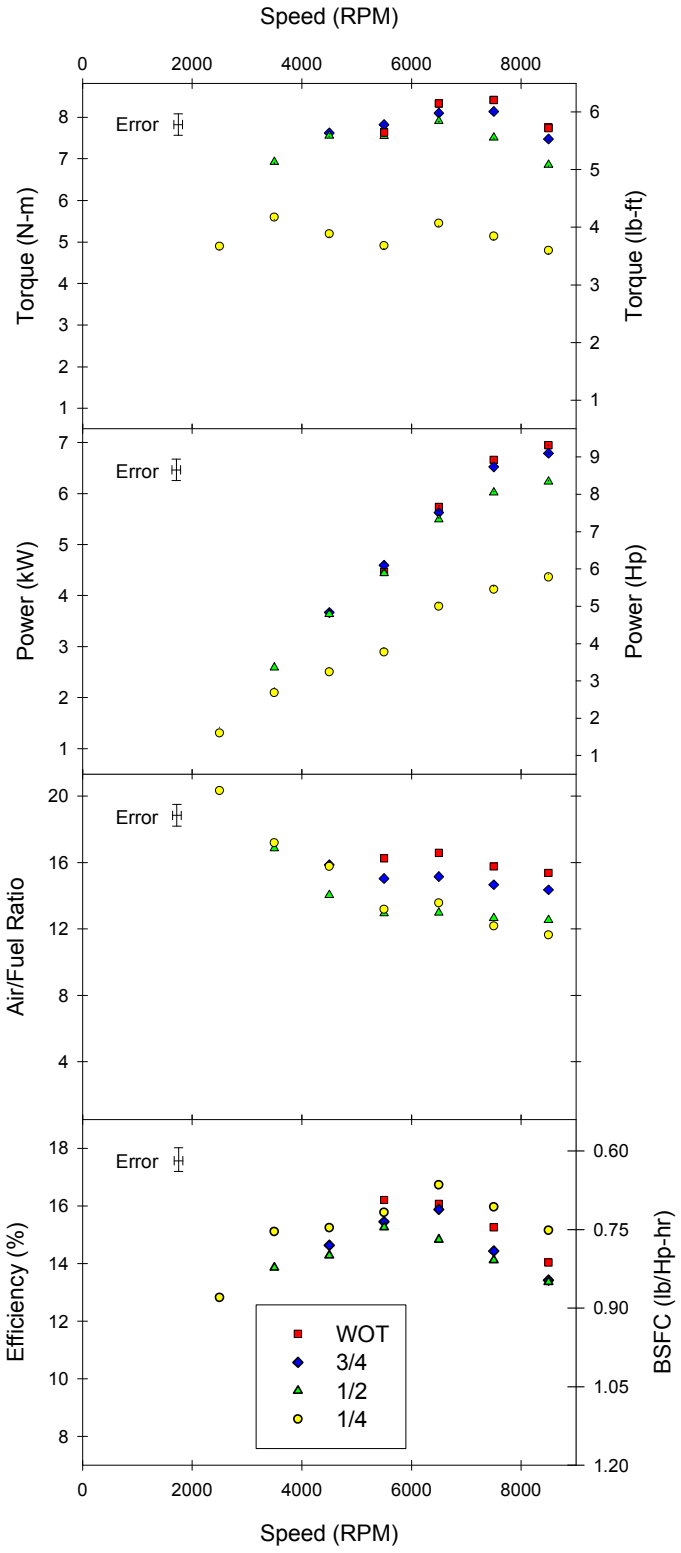

Figure 4.1: Engine Performance at various throttle settings

Figure 4.3 shows the gas concentration levels sampled from the engine's exhaust. Hydrocarbon, Carbon Monoxide, Carbon Dioxide, and Oxygen are plotted versus engine speed for different throttle settings. The results are consistent with the observations noted previously. CO concentration decreases with increasing throttle setting while CO_2 concentration increases. This makes sense because opening the throttle increases the availability of oxygen and facilitates the conversion of CO to CO_2. CO increases with engine speed because the gas temperature increases which in turn increases the rate at which CO_2 in the exhaust can dissociate back to CO.

The oxygen concentration decreases with increasing engine speed until about 5500 RPM because the fuel flow rate is increasing and more oxygen is being consumed to react with the fuel. Once the mixture ratio approaches stoichiometric conditions, the chemical reaction rate is near its maximum and the time required to complete chemical reaction is a constant value. Increasing the speed of the engine decreases the residence time of the mixture in the cylinder. As the engine speed increases, the Damkohler number [38] (defined as the ratio of the residence time to the chemical conversion time) decreases:

$$Da = \tau_T / \tau_L \qquad \text{(Eq. 4.1)}$$

Where τ_T is the residence time (length of time fuel/air mixture is in the cylinder after combustion has started) and τ_L is the chemical conversion time (length of time for fuel/air mixture to completely burn). The residence time starts at top dead center (TDC) or 360° when combustion begins and stops 100° later when the exhaust port is opened and the mixture exits the cylinder. The residence time is calculated from the known engine speed (X):

$$\tau_T = \left[X\left(\frac{rev}{1\min}\right) \times \left(\frac{1\min}{60\sec}\right) \right]^{-1} \times \left(\frac{100^\circ}{360^\circ}\right) \quad \text{(Eq. 4.2)}$$

While the chemical conversion time is calculated as follows:

$$\tau_L = \delta_L / S_L \quad \text{(Eq. 4.3)}$$

Where δ_L is the laminar flame thickness and S_L is the laminar flame speed (estimated values are δ_L = 0.2 mm and S_L =33 cm/s) [32]. When the Damkohler number approaches small values incomplete combustion begins to occur. A plot of the Damkohler number as a function of engine speed is shown in Figure 4.2.

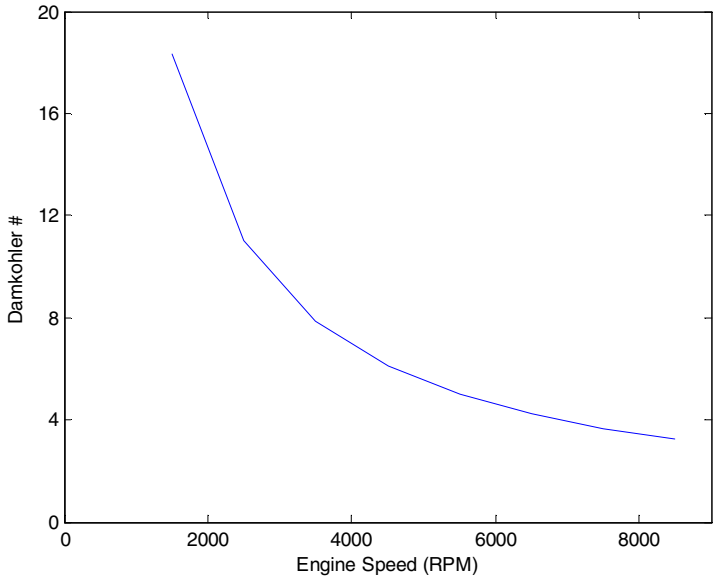

Figure 4.2: Damkohler number as a function of engine speed

Incomplete combustion means less chemical reaction has occurred and therefore more oxygen, more unburned hydrocarbons, and less CO_2 are present in the exhaust. The fact that unburned HC and O_2 concentrations begin to rise between 5500 and 6500 RPM (where Damkohler number is approximately 5) suggests that

incomplete combustion may be beginning in this region. Less combustion in the cylinder means less power produced and could partially explain why the efficiency of the engine peaks around 6000 RPM.

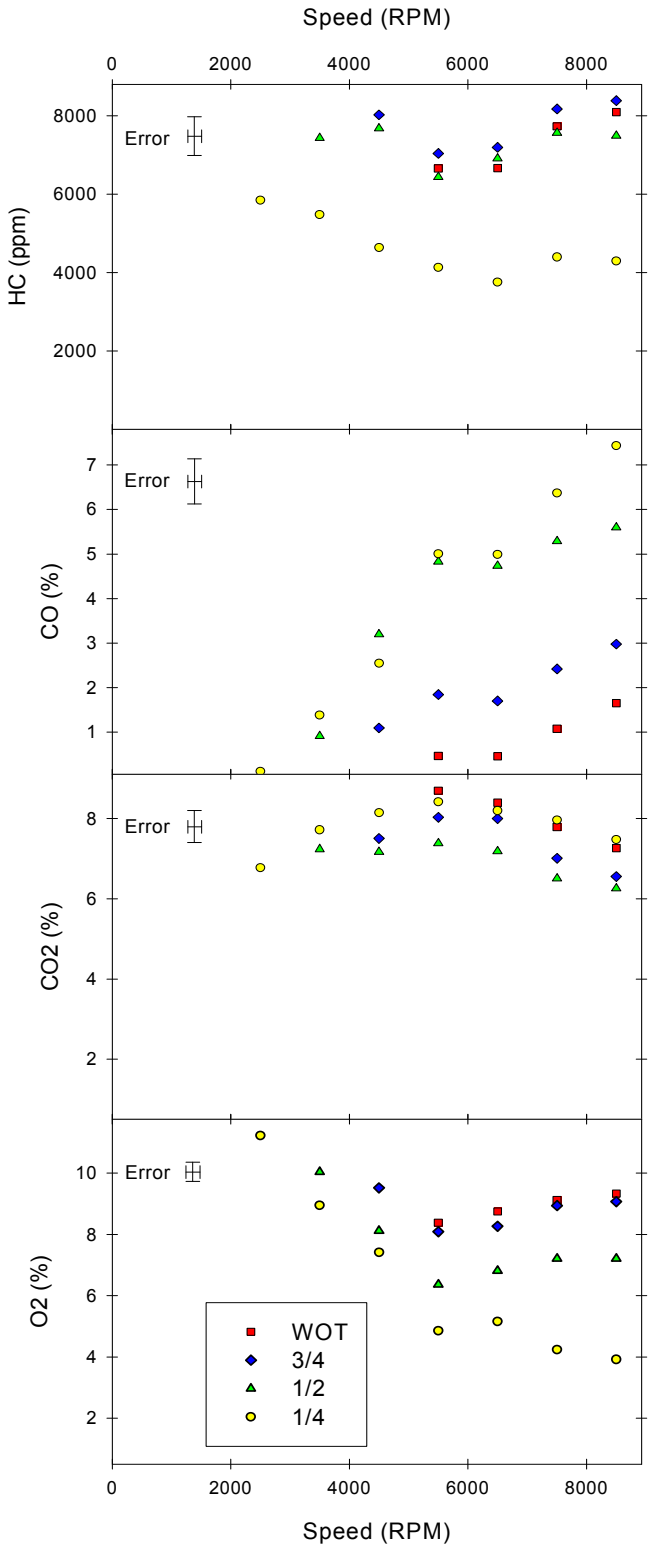

Figure 4.3: Exhaust gas concentrations at various throttle settings

Cylinder head and exhaust manifold temperatures (Figure 4.4) increase with increasing engine speed in this experiment because the cold-side thermal boundary conditions are fixed – the room temperature is constant as is the velocity of the air flow over the cylinder heads – while the fuel consumption (and hence the overall heat release rate) increases with engine speed. The differences between cylinder head and exhaust manifold temperatures at ¾ and WOT are small because the air/fuel ratio is relatively close to stoichiometric and combustion temperatures are relatively uniform. Decreasing the throttle setting lowers the air/fuel ratio below stoichiometric, which reduces the combustion temperature, and hence the temperature of the cylinder heads and exhaust manifold.

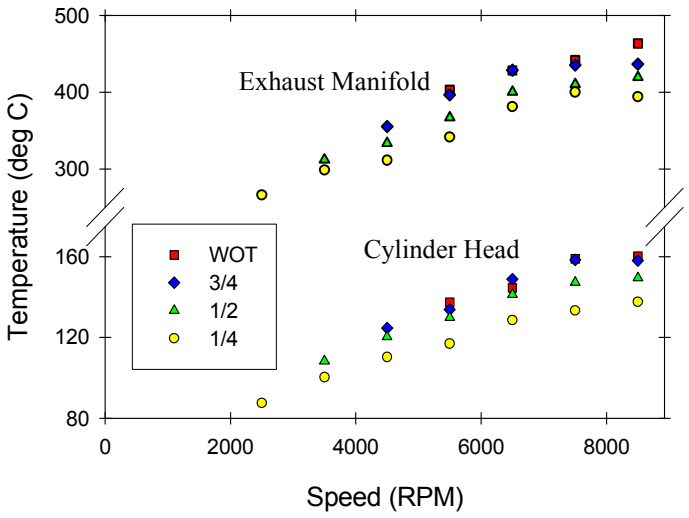

Figure 4.4: Cylinder head and exhaust manifold temperatures at various throttle settings

Throttle Position	Speed (RPM)	Uncertainty	Torque (lb-ft)	Uncertainty	Power (Hp)	Uncertainty	Air/Fuel Ratio	Uncertainty	Efficiency (%)	Uncertainty
WOT	8500	6.2	5.72	0.07	9.32	0.11	15.38	0.21	14.0	0.2
	7500	6.1	6.21	0.08	8.94	0.11	15.76	0.23	15.3	0.2
	6500	18.7	6.15	0.09	7.70	0.11	16.59	0.40	16.1	0.2
	5500	18.7	5.64	0.08	5.99	0.09	16.25	0.28	16.2	0.2
3/4	8500	5.2	5.51	0.07	9.11	0.10	14.36	0.26	13.4	0.1
	7500	4.8	6.00	0.07	8.75	0.10	14.66	0.29	14.4	0.2
	6500	7.1	5.98	0.07	7.54	0.09	15.15	0.35	15.9	0.2
	5500	8.4	5.77	0.07	6.16	0.08	15.04	0.20	15.5	0.2
	4500	14.3	5.62	0.08	4.92	0.07	15.86	0.10	14.6	0.2
1/2	8500	8.4	5.06	0.07	8.36	0.11	12.55	0.15	13.4	0.2
	7500	13.9	5.54	0.07	8.07	0.11	12.65	0.09	14.1	0.2
	6500	8.6	5.83	0.07	7.37	0.08	12.99	0.10	14.8	0.2
	5500	10.7	5.57	0.07	5.95	0.08	12.94	0.15	15.3	0.2
	4500	8.4	5.58	0.07	4.88	0.06	14.04	0.12	14.3	0.2
	3500	15.8	5.11	0.07	3.47	0.05	16.87	0.24	13.9	0.2
1/4	8500	16.6	3.54	0.07	5.85	0.11	11.64	0.18	15.2	0.3
	7500	15.5	3.79	0.08	5.53	0.11	12.17	0.26	16.0	0.3
	6500	24.1	4.02	0.11	5.08	0.14	13.56	0.46	16.7	0.5
	5500	38.1	3.62	0.11	3.88	0.12	13.18	0.29	15.8	0.5
	4500	9.5	3.83	0.06	3.36	0.06	15.77	0.24	15.2	0.3
	3500	17.0	4.13	0.07	2.81	0.05	17.18	0.47	15.1	0.3
	2500	41.5	3.61	0.18	1.75	0.09	20.33	0.27	12.8	0.7

Table 4.1: Engine performance data and associated uncertainties

Throttle Position	Speed (RPM)	Uncertainty	HC (ppm)	Uncertainty	CO (%)	Uncertainty	CO2 (%)	Uncertainty	O2 (%)	Uncertainty
WOT	8500	6.2	8096	404	1.65	0.09	7.26	0.36	9.33	0.50
	7500	6.1	7729	388	1.07	0.06	7.79	0.39	9.12	0.46
	6500	18.7	6665	336	0.45	0.03	8.40	0.42	8.74	0.44
	5500	18.7	6657	334	0.46	0.03	8.70	0.44	8.38	0.42
3/4	8500	5.2	8382	425	2.98	0.16	6.56	0.33	9.07	0.46
	7500	4.8	8176	411	2.42	0.12	7.01	0.35	8.94	0.45
	6500	7.1	7195	362	1.70	0.09	8.00	0.40	8.26	0.41
	5500	8.4	7040	356	1.84	0.10	8.03	0.41	8.08	0.41
	4500	14.3	8023	405	1.09	0.06	7.50	0.38	9.52	0.48
1/2	8500	8.4	7489	382	5.60	0.29	6.26	0.31	7.21	0.36
	7500	13.9	7563	382	5.29	0.27	6.50	0.32	7.20	0.36
	6500	8.6	6912	349	4.74	0.25	7.19	0.36	6.81	0.34
	5500	10.7	6433	326	4.83	0.25	7.38	0.37	6.36	0.32
	4500	8.4	7677	387	3.19	0.17	7.17	0.36	8.12	0.41
	3500	15.8	7439	378	0.91	0.05	7.23	0.37	10.04	0.51
1/4	8500	16.6	4291	216	7.43	0.38	7.47	0.38	3.91	0.20
	7500	15.5	4393	224	6.36	0.34	7.96	0.41	4.23	0.21
	6500	24.1	3753	192	4.99	0.27	8.20	0.42	5.15	0.26
	5500	38.1	4132	210	5.00	0.27	8.41	0.43	4.84	0.25
	4500	9.5	4639	235	2.54	0.14	8.14	0.41	7.40	0.38
	3500	17.0	5474	282	1.38	0.08	7.72	0.39	8.94	0.45
	2500	41.5	5846	299	0.11	0.01	6.77	0.35	11.22	0.57

Table 4.2: Emissions data and associated uncertainties

Chapter 5: Engine Simulation

5.1 Configuration

An attempt was also made to simulate the 3W 100i-B2 engine using a custom written computer code based on MatLab software. MatLab was utilized to solve the coupled set of ordinary differential equations (ODE's) describing heat, mass, and momentum exchange within the cylinder and crankcase. These equations are solved simultaneously and integrated over one engine cycle with respect to the crank angle.

The equations that govern what is physically occurring inside the engine include the equation of state for an ideal gas, the first and second laws of thermodynamics, conservation of mass and energy, work output, and a forcing term which in this case is the change in cylinder volume as a function of time. The equation of state for a perfect gas is given as:

$$PV = mRT \qquad \text{(Eq. 5.1)}$$

Where P, V, m, and T are the pressure, volume, mass, and temperature of the gas. R is the specific gas constant and has a value of 287 J/(kg-K) for air at standard atmospheric conditions. The first law of thermodynamics relates the change in energy (dE) in the system (engine) to the amount of heat transferred (dQ) and the amount of work done (dW).

$$dE = dQ - dW \qquad \text{(Eq. 5.2)}$$

The second law of thermodynamics states that processes must occur in a certain direction and that leads to the increase of entropy principle:

$$dS \geq \frac{dQ}{T} \qquad \text{(Eq. 5.3)}$$

Where dS is the change in entropy, dQ is the net heat flux to the system, and T is the temperature of the system. The net heat flux to the system (dQ) is equal to the heat input (Q_{in}) minus the heat lost (Q_{out}).

$$dQ = Q_{in} - Q_{out} \qquad \text{(Eq. 5.4)}$$

Conservation of mass states that any change in mass (dm) within the system must equal the amount of incoming mass (m_{in}) minus the amount of mass leaving the system (m_{out}).

$$dm = m_{in} - m_{out} \qquad \text{(Eq. 5.5)}$$

The work output from the system is determined by multiplying the pressure and the change in volume:

$$dW = PdV \qquad \text{(Eq. 5.6)}$$

The complete system of equations in matrix form as shown in Figure 5.1 is solved simultaneously for both the cylinder and the crankcase.

$$\begin{array}{c} \\ State \\ Mass \\ Work \\ Energy \\ Forcing \\ 1^{st}\,Law \\ 2^{nd}\,Law \end{array} \begin{bmatrix} V & -RT & 0 & 0 & P & -mR & 0 \\ 0 & 1 & 0 & 0 & 0 & 0 & 0 \\ 0 & 0 & 1 & 0 & -P & 0 & 0 \\ 0 & 0 & 0 & 1 & 0 & 0 & 0 \\ 0 & 0 & 0 & 0 & 1 & 0 & 0 \\ 0 & 0 & 1 & -1 & 0 & mC_v & 0 \\ 0 & 0 & 0 & -1/T & 0 & 0 & 1 \end{bmatrix} \frac{d}{d\theta} \begin{bmatrix} P \\ m \\ W \\ Q \\ V \\ T \\ S \end{bmatrix} = \begin{bmatrix} 0 \\ (\dot{m}_{in} - \dot{m}_{out})/\omega \\ 0 \\ (\dot{Q}_{in} - \dot{Q}_{out})/\omega \\ A \\ 0 \\ 0 \end{bmatrix}$$

Figure 5.1: System of governing equations

The user specifies the engine dimensions, fuel and air parameters, environmental conditions, thermodynamic properties, and initial conditions inside the engine. The program then outputs pressure, volume, temperature, charge mass, heat content, and internal energy as a function of the crank angle as well as a pressure-volume (PV) diagram. The indicated power of the engine can be calculated by integrating the PV curve to obtain the indicated work per cycle [32]:

$$W_{c,i} = \oint p dV \qquad \text{(Eq. 5.7)}$$

In this equation, p is the instantaneous pressure inside the cylinder and dV is the change in volume per crank angle degree. Since the engine being tested has two cylinders and the program is setup to handle a single cylinder engine, the values calculated are for one cylinder while the indicated power is calculated by doubling the computed work. The indicated power is given by the following equation:

$$P_i = \frac{W_{c,i} N}{n_R} \qquad \text{(Eq. 5.8)}$$

Where N is the crankshaft rotational speed and n_R is the number of crank revolutions per power stroke. In this case, for a two-stroke engine, n_R equals 1. The indicated power differs from the brake power because it does not include the power required to overcome the effects of friction inside the engine due to the piston-cylinder interaction, bearings, etc. and the power needed to drive engine accessories. For that reason, the indicated power is always greater than the brake power. This can be seen from the following equation:

$$P_i = P_b + P_f \qquad \text{(Eq. 5.9)}$$

Where P_i is the indicated power which is the power the engine would produce in an ideal situation where there is no friction or other power losses associated with operating the engine, P_b is the brake power which is the power that the engine makes in the 'real world' and what is measured on the dynamometer, and P_f is the power required to overcome friction. The mechanical efficiency of the engine is given by:

$$\eta_m = \frac{P_b}{P_i} = 1 - \frac{P_f}{P_i} \qquad \text{(Eq. 5.10)}$$

For the purposes of comparing the simulation's predictions to the dynamometer measurements, the engine is assumed to have a 75% mechanical efficiency at WOT which is a reasonable value for this type of engine [32]. Based on this assumption and the brake power (9.32 Hp) obtained from experimental testing, the indicated power for this engine was calculated to be 12.43 Hp.

5.2 Results

While the simulation results exhibited the correct trends, the magnitudes of torque, power, etc. predicted did not match experimental values. Therefore, scaling factors were implemented so that the numerical results would resemble the performance of the actual engine. *In view of that fact, the intent here is not to predict the actual performance of the engine but rather to use the simulation to examine the effects of changing operating parameters on the engine's performance.*

The simulation was used to run calculations corresponding to WOT at the engine's maximum operating speed of 8500 RPM. These calculations were performed to establish a set of values to be used as a baseline for comparison when the engine's parameters are changed. The parameters that are adjusted for this

particular simulation include, but are not limited to, the following: transfer port timing and duration, exhaust port timing and duration, and ignition timing. An in-depth analysis is used to discuss likely reasons for the increase or decrease in performance. The analysis incorporates figures used to characterize the baseline case which include property values in both the cylinder and crankcase while the figures corresponding to modified cases display the properties in the cylinder.

The results from the simulation, as seen if Figure 5.2, show that the effect on indicated power output due to the parameter variation is minimal suggesting the engine is quite optimized.

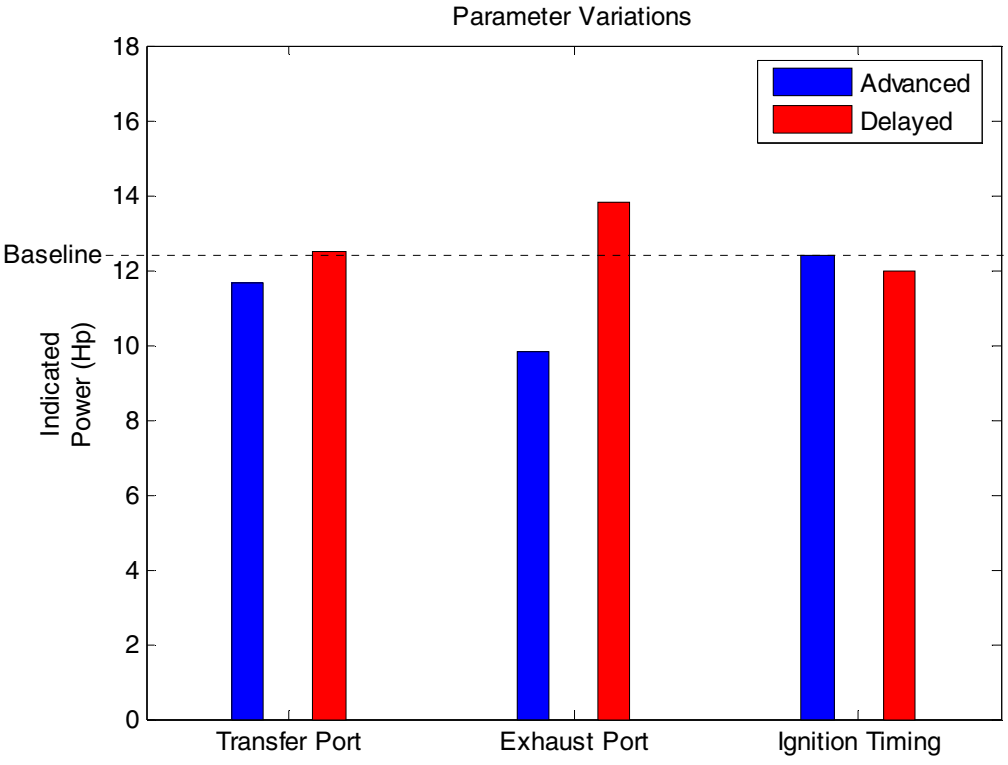

Figure 5.2: Effect of parameter variations on indicated power

Delaying the time that the transfer port opens shows a negligible gain in power, while advancing the time results in a decrease in power output (~ 0.75 Hp). Advancing the exhaust port timing also decreased the power output, this time by a substantial amount (~ 2.5 Hp). However, delaying the exhaust port timing resulted in a modest power gain (~1.5 Hp) signifying that it may be possible to increase the engine's performance by shortening the length of time that the exhaust port is open. The simulation also indicates there is no potential gain in performance by advancing or delaying the ignition timing as each modification caused a slight decrease in power output.

5.3 Baseline Analysis

Figure 5.3 shows the cylinder and crankcase volumes over the entire engine cycle as the piston moves from bottom dead center (BDC) at 180° to top dead center (TDC) at 360° and then back to BDC. The figure shows that the program displays the correct values and behavior for the changes in volume with respect to the crank angle.

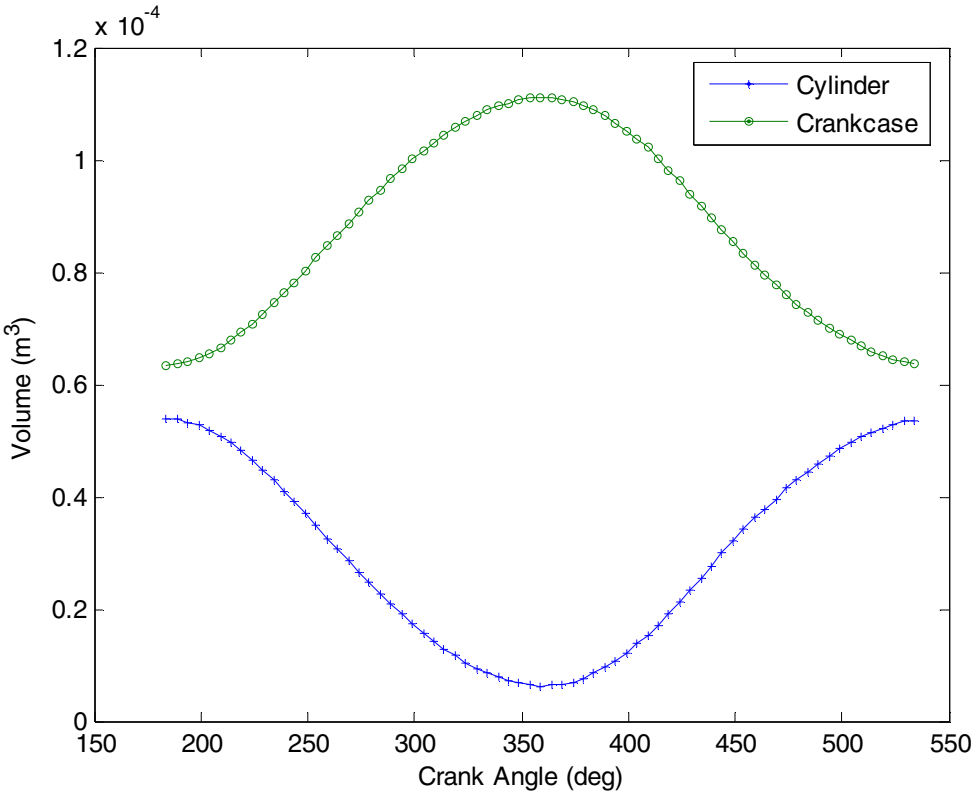

Figure 5.3: Cylinder and crankcase volume for 3W 100i-B2

Figure 5.4 shows the pressure ratio as a function of crank angle. The cylinder pressure increases during the compression stroke as the piston moves toward the top (TDC). At 360° or TDC there is a large spike in pressure attributed to heat release due to combustion of the fuel/air mixture. The combustion process is modeled as a linear heat release curve using the heating value and mass of the fuel in the cylinder. The exact duration of combustion in the engine is unknown so a 10° interval is assumed. The pressure ratio attains a maximum value of roughly 49 at about 370° or 10° after TDC assuming combustion has completed and then decreases with the expansion or power stroke.

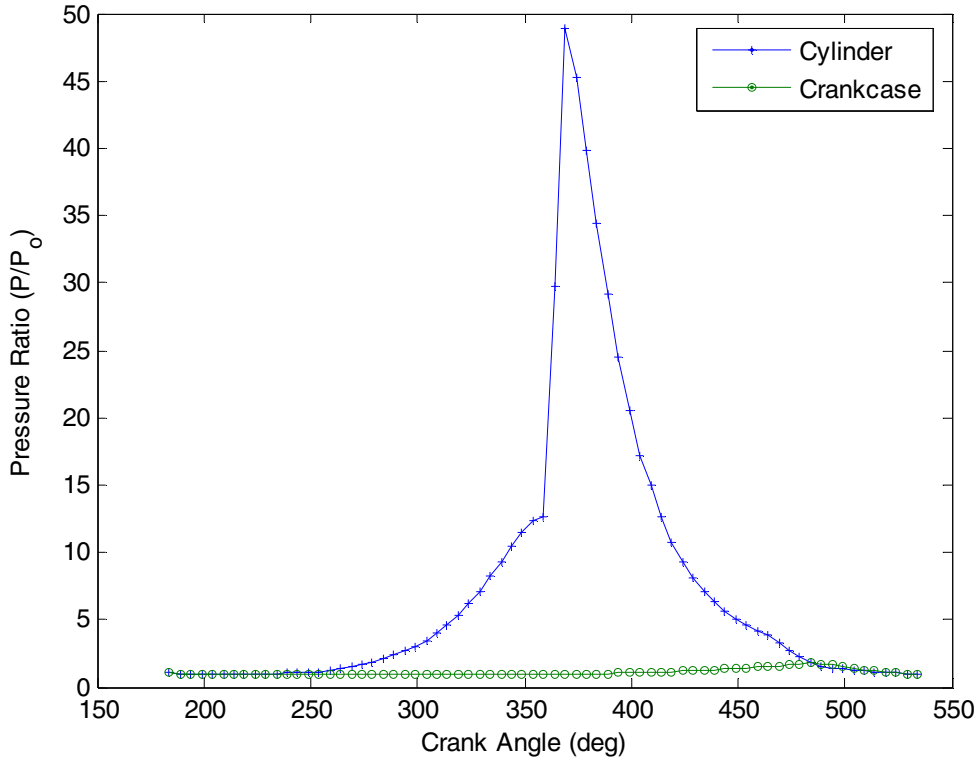

Figure 5.4: Pressure ratio at WOT and engine speed of 8500 RPM

Figure 5.5 shows the charge temperature as a function of crank angle. As can be seen there is a slight increase in temperature as the piston moves toward TDC. This is due to the compression of the charge in the cylinder. At TDC, the temperature experiences a sharp increase due to the heat release from combustion. After reaching a peak value of slightly over 2000 K, the temperature then decreases during expansion until the exhaust port opens at 460°. After the port opens, the temperature decreases at a faster rate due to the gases escaping from the exhaust port.

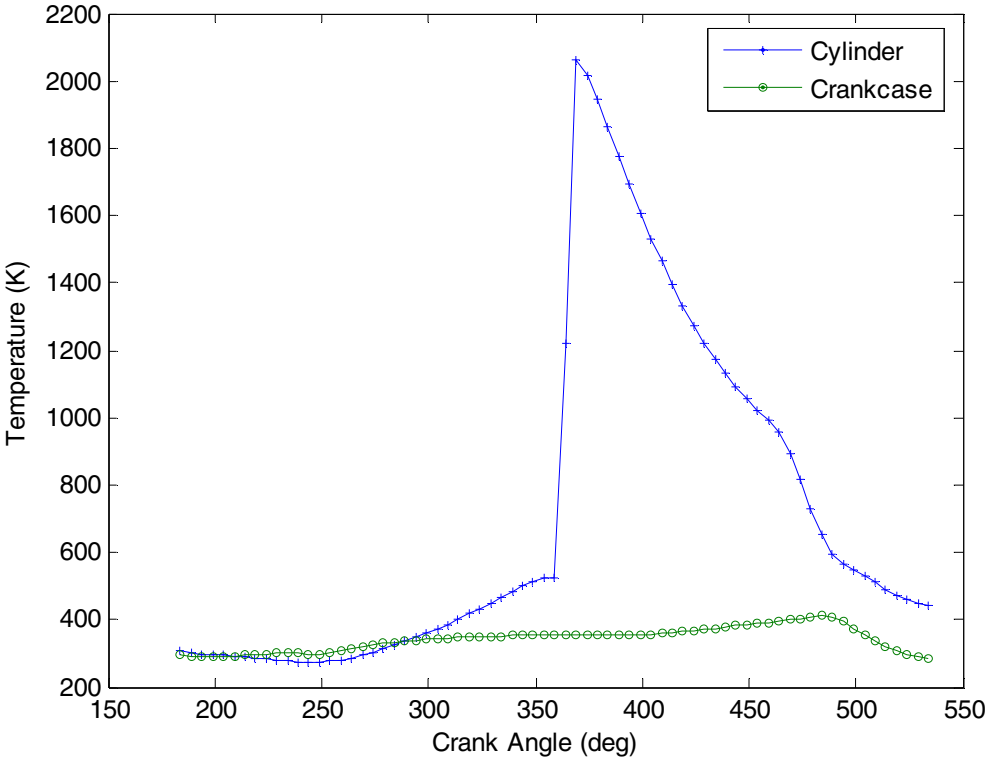

Figure 5.5: Temperature at WOT and engine speed of 8500 RPM

The charge mass is shown in Figure 5.6. At BDC, the charge mass decreases in the cylinder until the piston reaches 260°. This is because the exhaust port is still open which allows a portion of the incoming charge mass to flow out of the cylinder along with the exhaust gases. After 260°, the charge mass stays constant in the cylinder since both the transfer and exhaust ports are closed. The mass remains constant until the exhaust port opens again at 460°. The crankcase on the other hand, has an increase in charge mass from BDC to TDC. This is because the upward motion of the piston increases the crankcase volume. This lowers the pressure in the crankcase drawing air through the carburetor and a fresh charge into the crankcase. The charge stored in the crankcase compresses when the piston begins to move down

causing the intake valve to close. When the transfer port opens at 480°, the pressurized fresh charge flows from the crankcase into the cylinder.

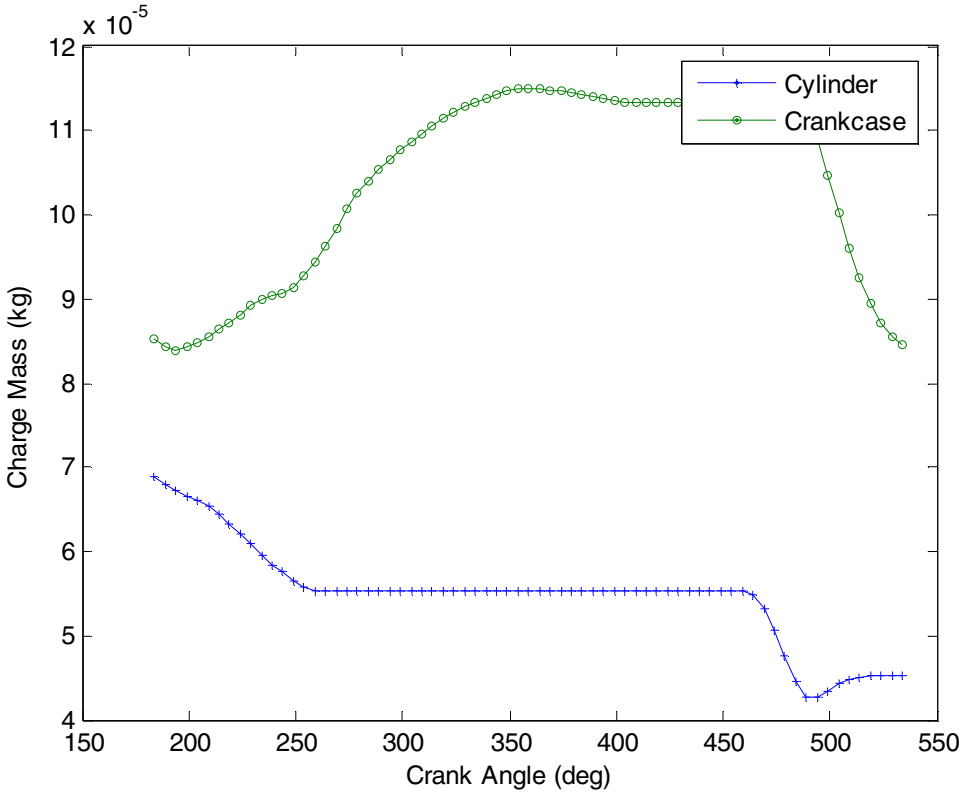

Figure 5.6: Charge mass at WOT and engine speed of 8500 RPM

Figure 5.7 and 5.8 show the enthalpy and internal energy inside the engine. Both plots show that as combustion occurs, there is a spike in both the enthalpy and internal energy associated with the fuel being burned.

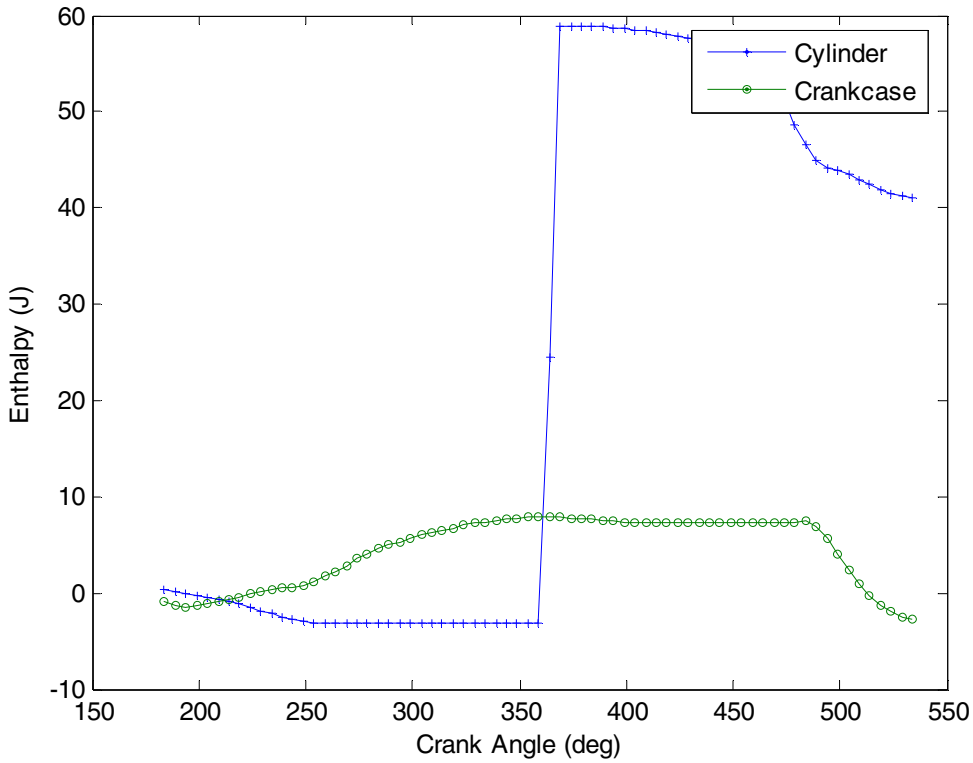

Figure 5.7: Enthalpy at WOT and engine speed of 8500 RPM

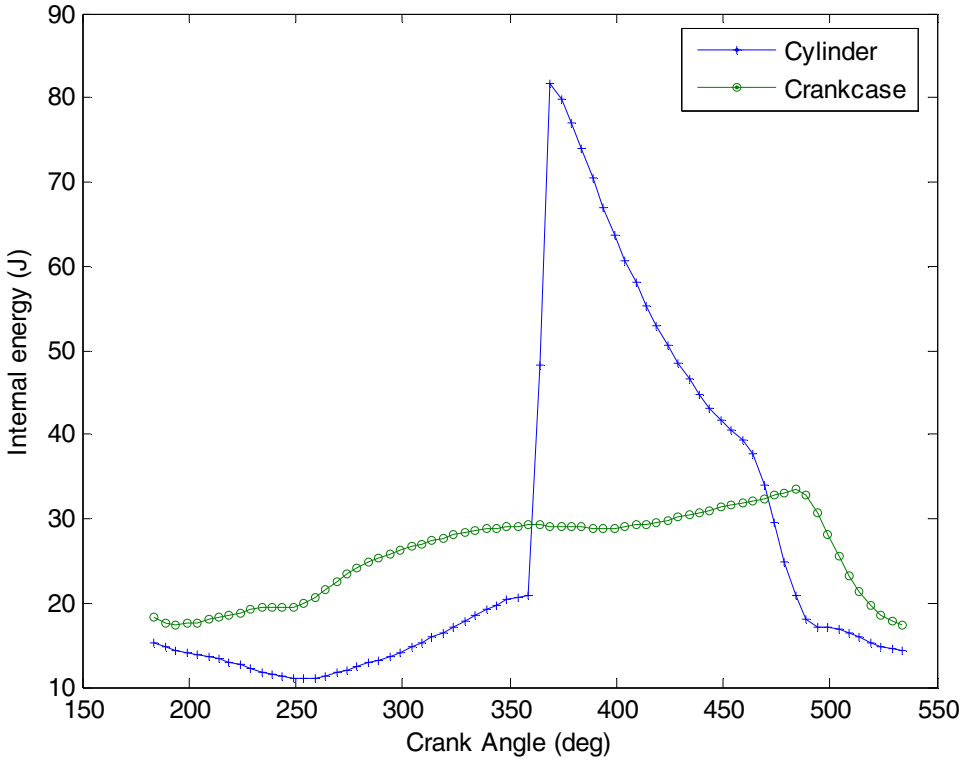

Figure 5.8: Internal energy at WOT and engine speed of 8500 RPM

Figure 5.9 is a PV diagram of the charge in the cylinder. As stated earlier, the area enclosed by the curve represents the amount of work produced by the engine. The area divided by the time required to complete the cycle (proportional to engine speed) gives the indicated power.

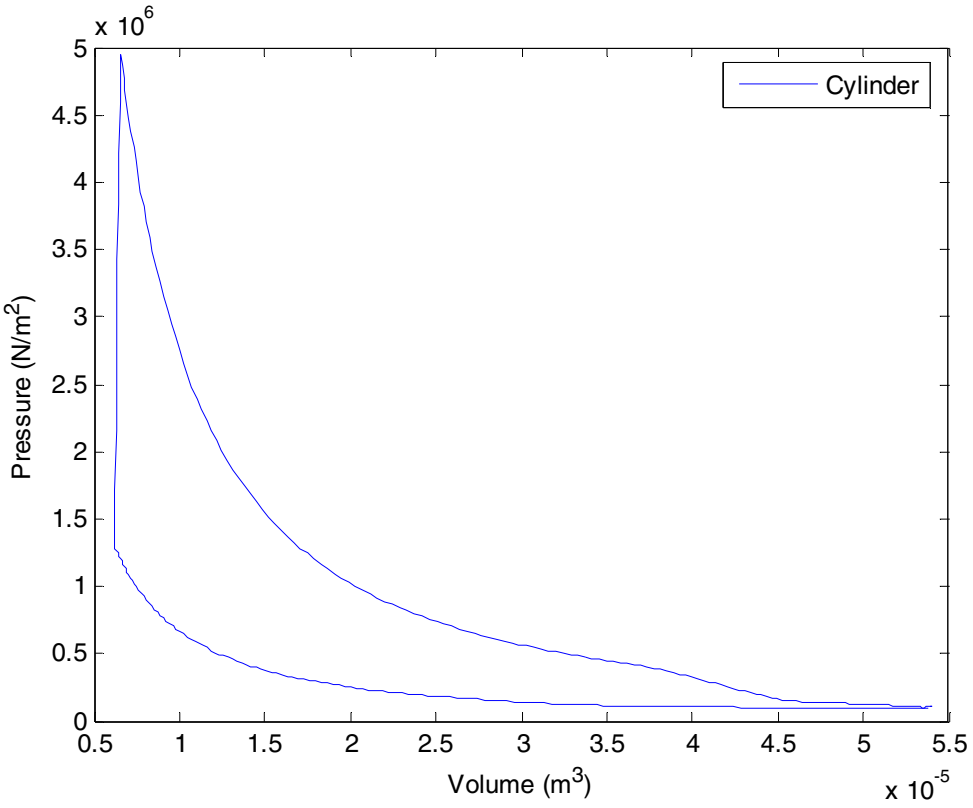

Figure 5.9: PV diagram for WOT and engine speed of 8500 RPM

Figure 5.10 shows the power and torque curves for the engine at WOT predicted using the simulation. The engine's speed was varied and new values for power were calculated each time the program was run. The torque values were then computed from the power and speed. The plot shows a linear increase in power from idle at 1500 RPM all the way up to the maximum operating speed of 8500 RPM. Meanwhile the torque remains fairly constant at approximately 7 to 7.5 lb-ft. The largest power output of 12.43 Hp is shown to occur at the maximum operating speed.

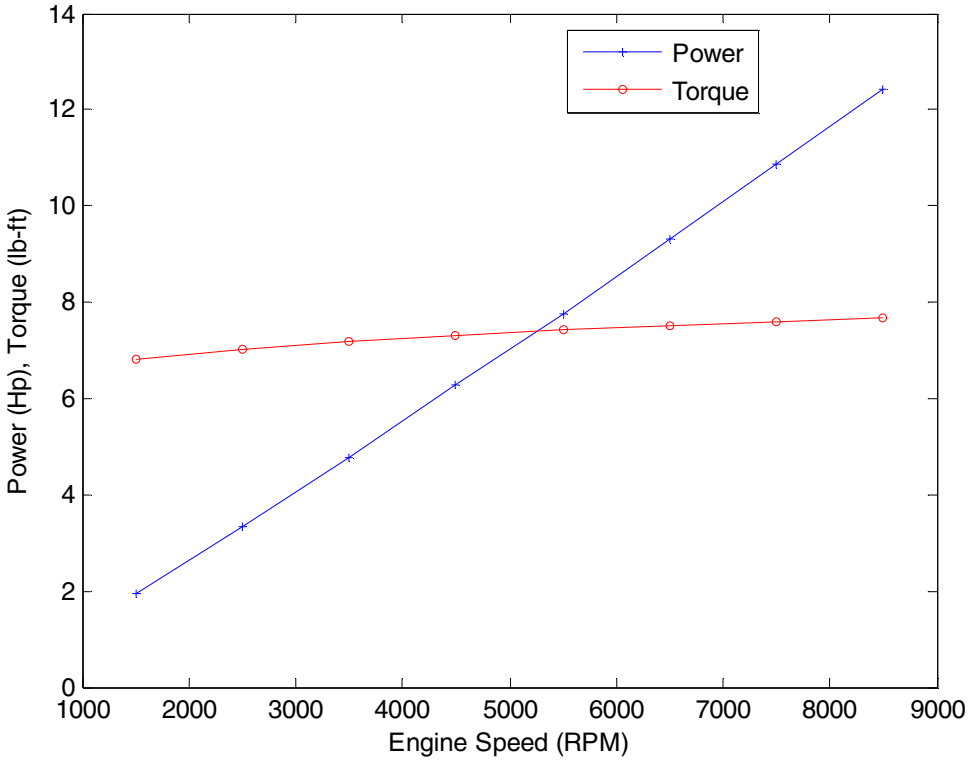

Figure 5.10: Power and torque curves at WOT

5.4 Parameter Variation Analysis

The first parameter to be adjusted was the transfer port timing and duration. The timing of the port's opening was advanced and delayed by 20° from its current point to effectively increase and decrease the length of time that the port is open. As seen in Figure 5.11, the pressure is lower throughout the cycle when the transfer port is opened sooner and closed later (increased duration). A possible explanation could be a reverse flow of the fresh charge into the crankcase since the transfer port closes after the compression stroke has started. As the piston moves to TDC, the pressure in the cylinder becomes greater than the pressure in the crankcase causing some of the

fresh charge to flow back into the crankcase. The longer the transfer port is held open, the greater the reverse flow is into the crankcase leaving a smaller amount of fresh charge in the cylinder for combustion. When the port duration is decreased, the pressure closely follows the baseline profile suggesting the current configuration is approximately optimum.

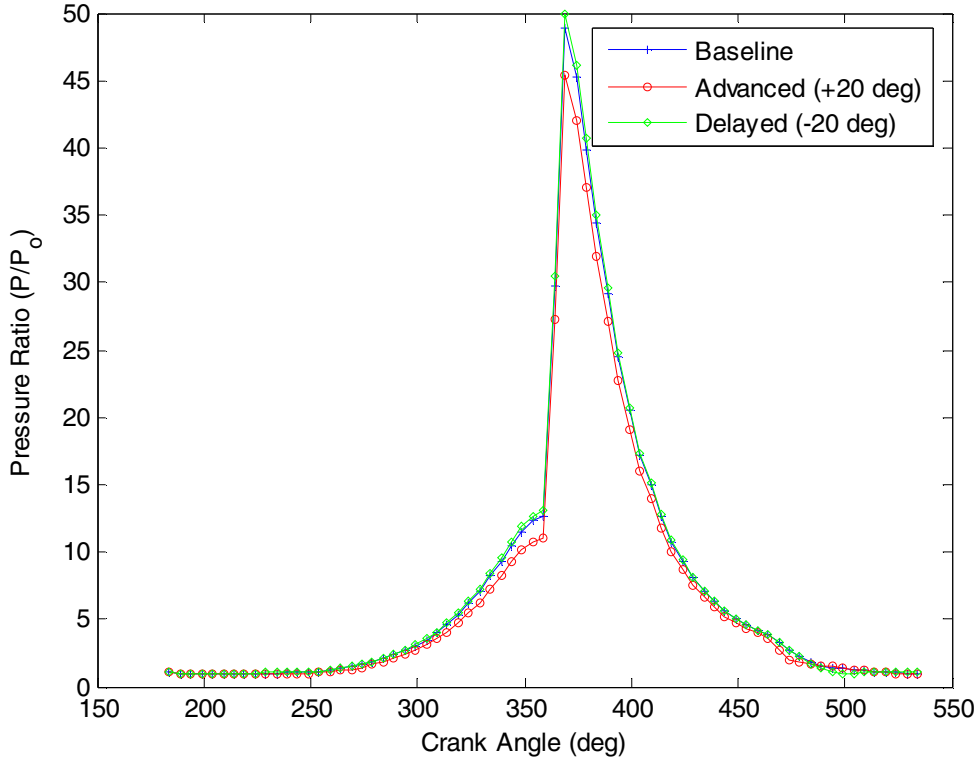

Figure 5.11: Effect of transfer port opening duration on pressure ratio

Figure 5.12 shows the effect of changing the timing and duration of the transfer port opening on the cylinder gas temperature. The behavior is similar to the pressure: as the time increases in which the port is open, the temperature decreases slightly across the entire cycle. Also note that since the transfer port opens earlier,

the temperature experiences a visible drop at 460° compared to the other profiles. This is probably due to the exhaust and transfer ports opening at the same time compared to the other configurations where the exhaust port opens before the transfer. Having both ports open at the same time allows the hot exhaust gases to escape and the fresh charge which lowers the temperature in the cylinder at a faster rate. On the other hand, a decrease in port duration does not have much of an effect on the temperature when compared with its current state.

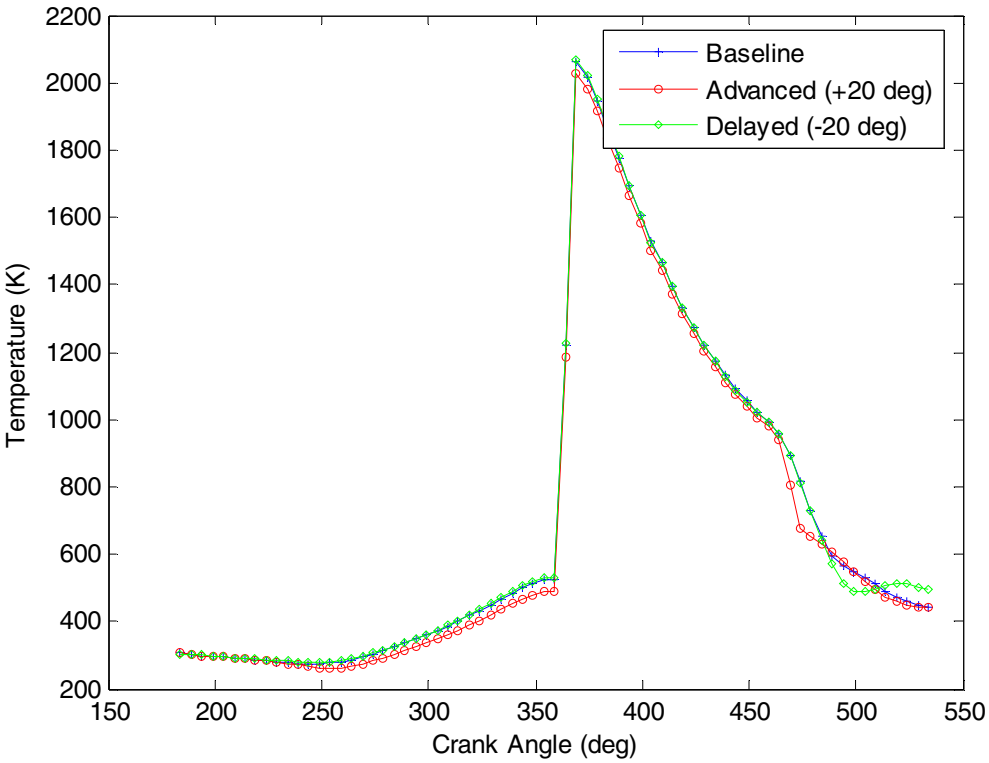

Figure 5.12: Effect of transfer port opening duration on temperature

Figure 5.13 shows the charge mass profiles for the different transfer port timing and durations. Again, the effect of transfer port timing shows the same general trend as with the temperature and pressure plots.

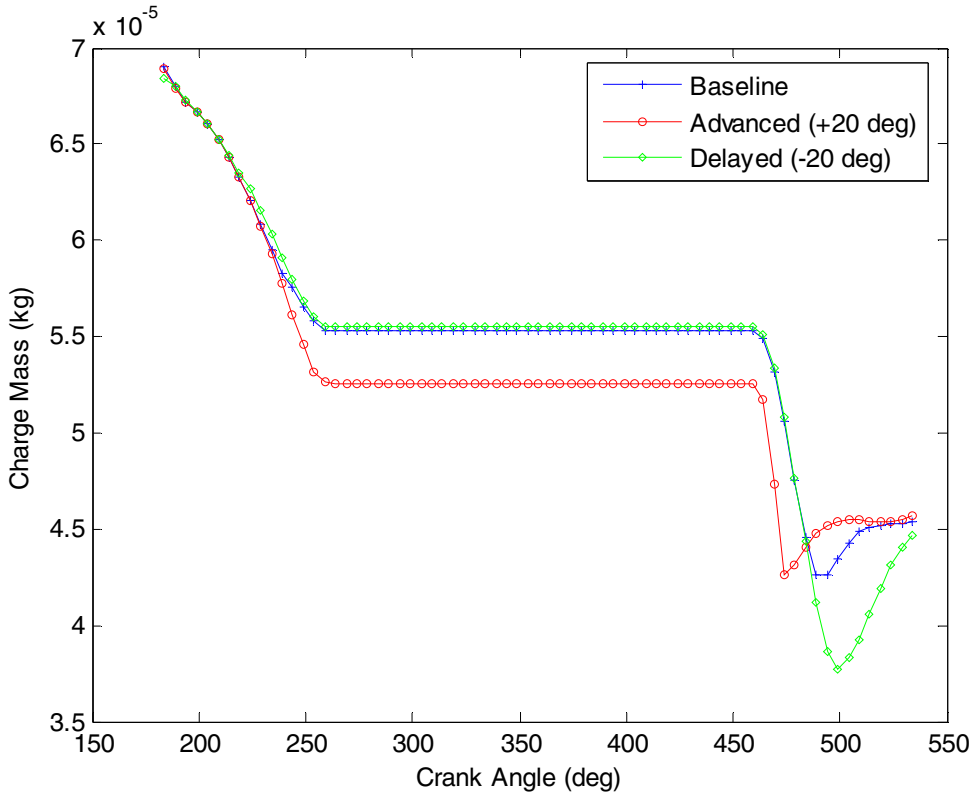

Figure 5.13: Effect of transfer port opening duration on charge mass

Figure 5.14 shows PV diagrams for the different transfer port timings. The area under each curve was integrated for each to compute the indicated power. The indicated power decreased from the baseline estimate of 12.43 Hp to 11.66 Hp for the increased port duration, while decreasing the duration saw a very slight increase to 12.48 Hp.

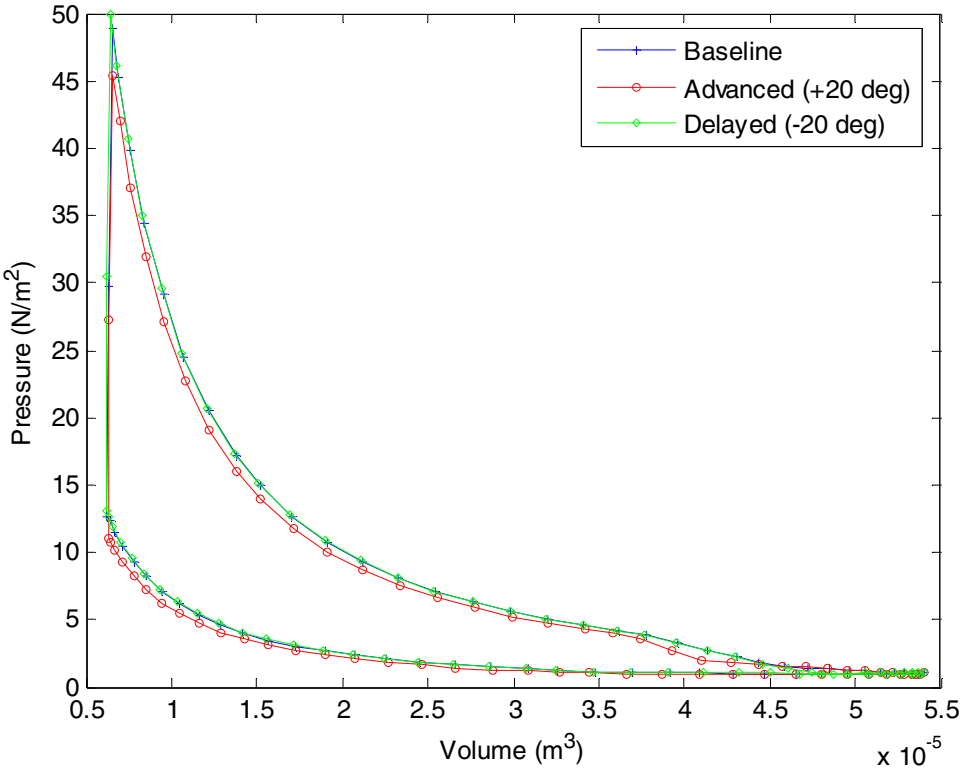

Figure 5.14: PV diagram for different transfer port opening durations

The next parameter to be adjusted was the exhaust port timing and duration. The timing of the port's opening was also advanced and delayed by 20° from its current point to effectively increase and decrease the length of duration that the exhaust port is open. As seen in Figure 5.15, the pressure profiles follow a similar pattern to when the transfer port was adjusted. When the exhaust port duration is increased, the pressure ratio drops but if the duration is decreased then the peak pressure ratio increases.

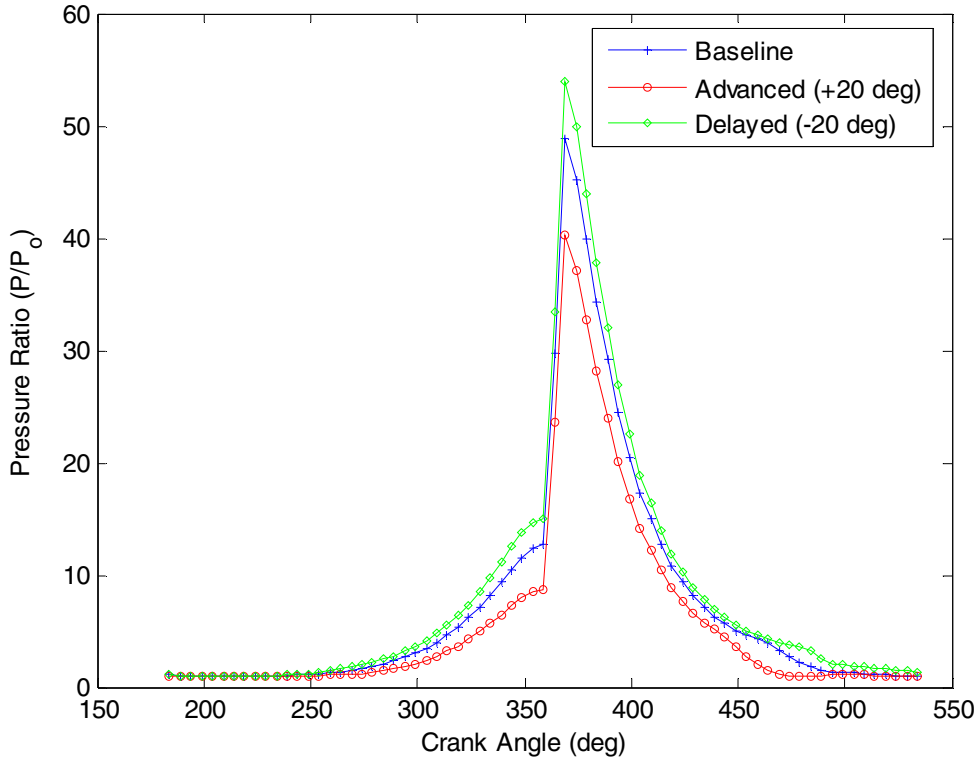

Figure 5.15: Effect of exhaust port opening duration on pressure ratio

Figure 5.16 shows the cylinder gas temperature for varying exhaust port timing and duration. Again, the pattern is similar to that seen in the temperature profiles when the transfer port was adjusted. Increasing the time that the port is open lowers the temperature, while decreasing the port duration increases the temperature. The effect of changing the exhaust port timing is evident by examining the rate and time at which the temperature decreases during the expansion stroke. The sooner the exhaust port is opened, the earlier the temperature starts to decrease. It also increases the rate at which it decreases.

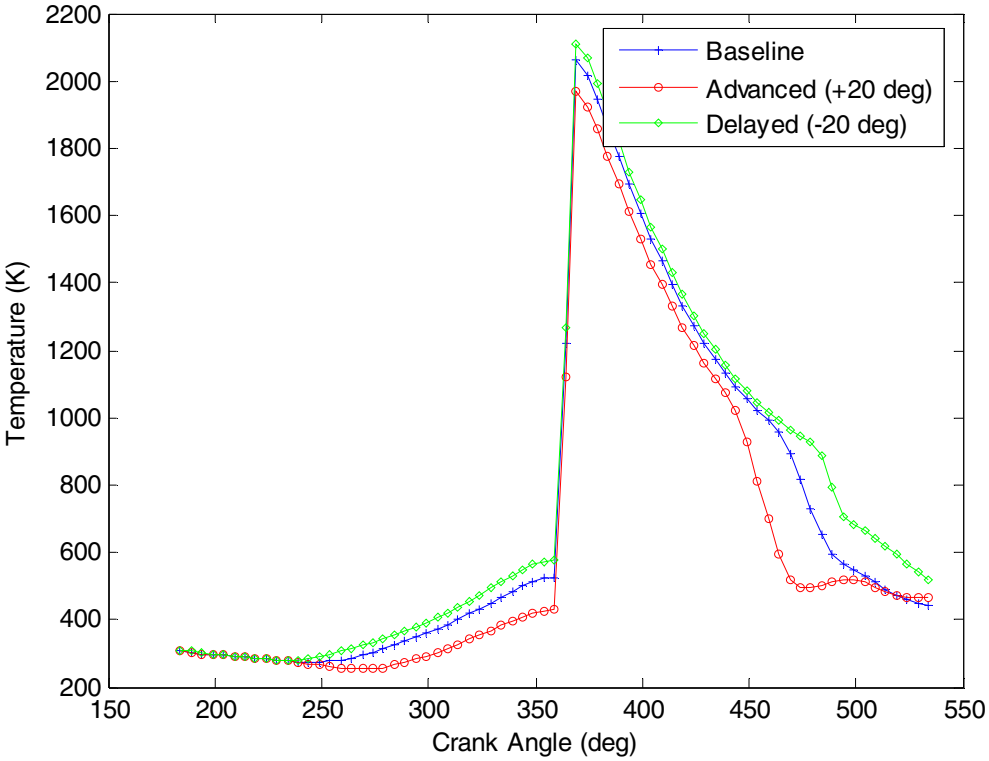

Figure 5.16: Effect of exhaust port opening duration on temperature

Figure 5.17 shows the effects on charge mass for varying lengths of exhaust port duration. From the plot, it shows that the exhaust port timing has a stronger impact on the amount of mass available for combustion than the transfer port timing. Because the engine scavenges the exhaust gas with the fresh charge (the incoming fuel-air mixture is used to help push the exhaust gas out of the cylinder), a portion of the fresh charge will flow out the exhaust port along with the exhaust gas. As the exhaust port is left open longer, it allows more fresh charge to flow out. This 'short circuiting' lowers the amount of fresh charge mass left in the cylinder.

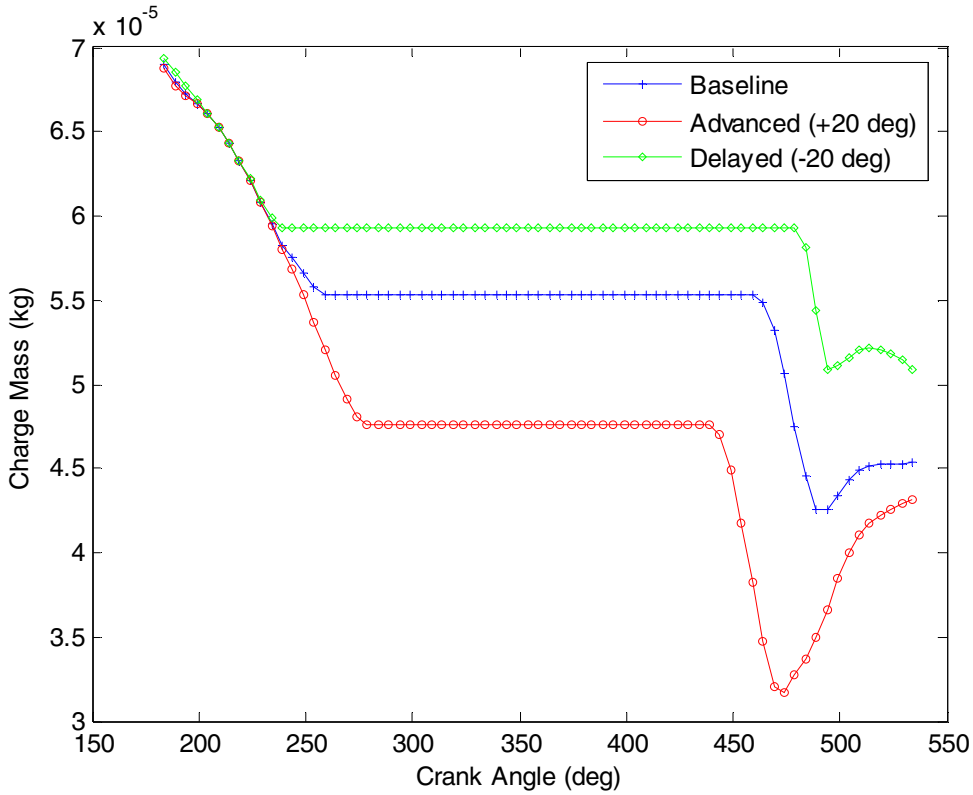

Figure 5.17: Effect of exhaust port opening duration on charge mass

Figure 5.18 shows PV diagrams for the different exhaust port timing and durations. The area under each curve was integrated to find the indicated power. The indicated power decreased from the baseline estimate of 12.43 Hp to 9.84 Hp for the increased port duration, while decreasing the duration saw an increase to 13.8 Hp. The exhaust port timing and duration seems to have a stronger influence on the engine's performance than the transfer port timing and duration.

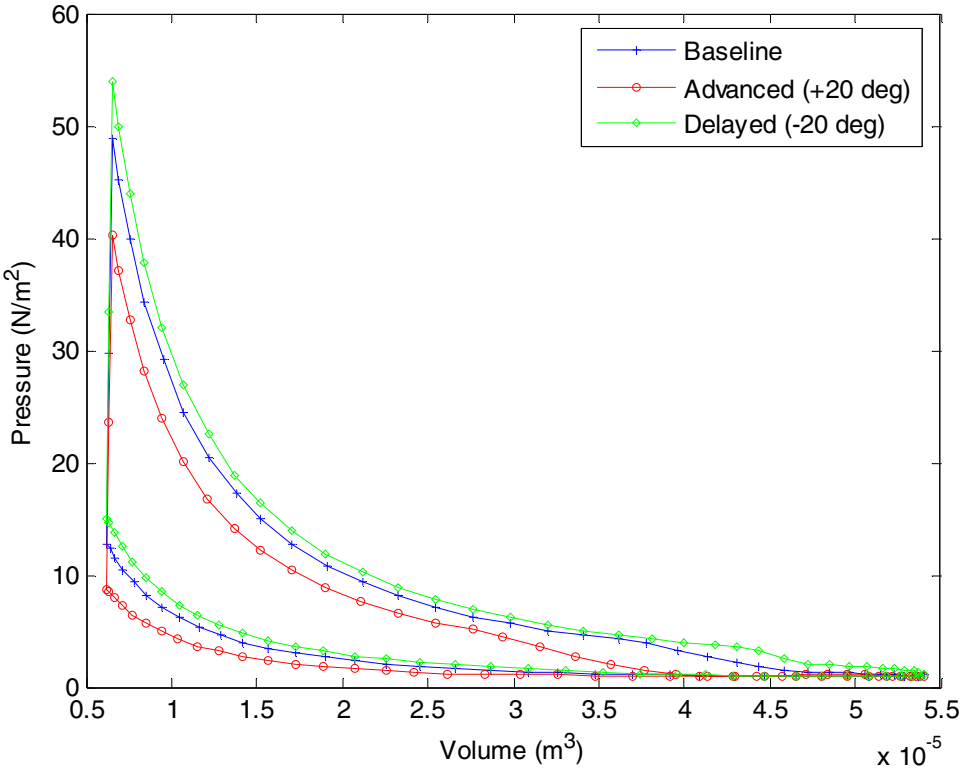

Figure 5.18: PV diagram for different exhaust port durations

The next parameter to be adjusted is the ignition timing which determines the starting point for the combustion process. The ignition timing is advanced and retarded by 10° from the current angle of 360° or TDC. Figure 5.19 shows the effects of changing the timing on the cylinder pressure. By advancing the ignition, the pressure not only peaks earlier but also slightly higher at a ratio of approximately 52 compared to the baseline ratio of 49. When the ignition is retarded, the pressure drops to a ratio of approximately 41. The temperature profiles behave similarly as shown in Figure 5.20. As the ignition is advanced, the temperature peaks earlier and higher than in the baseline case, and is lower when the ignition timing is retarded. However, the change in temperature is relatively small, with approximately a 40 K

increase with advance and a 55 K decrease with retard in ignition with respect to the baseline peak temperature of approximately 2060 K.

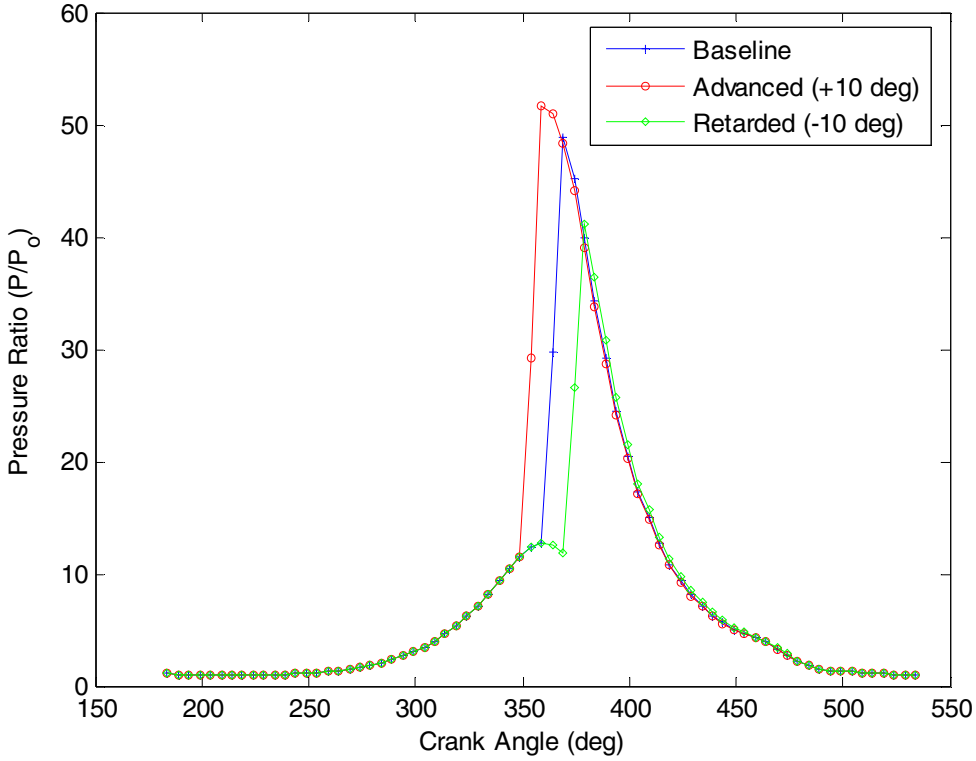

Figure 5.19: Effect of ignition timing on pressure ratio

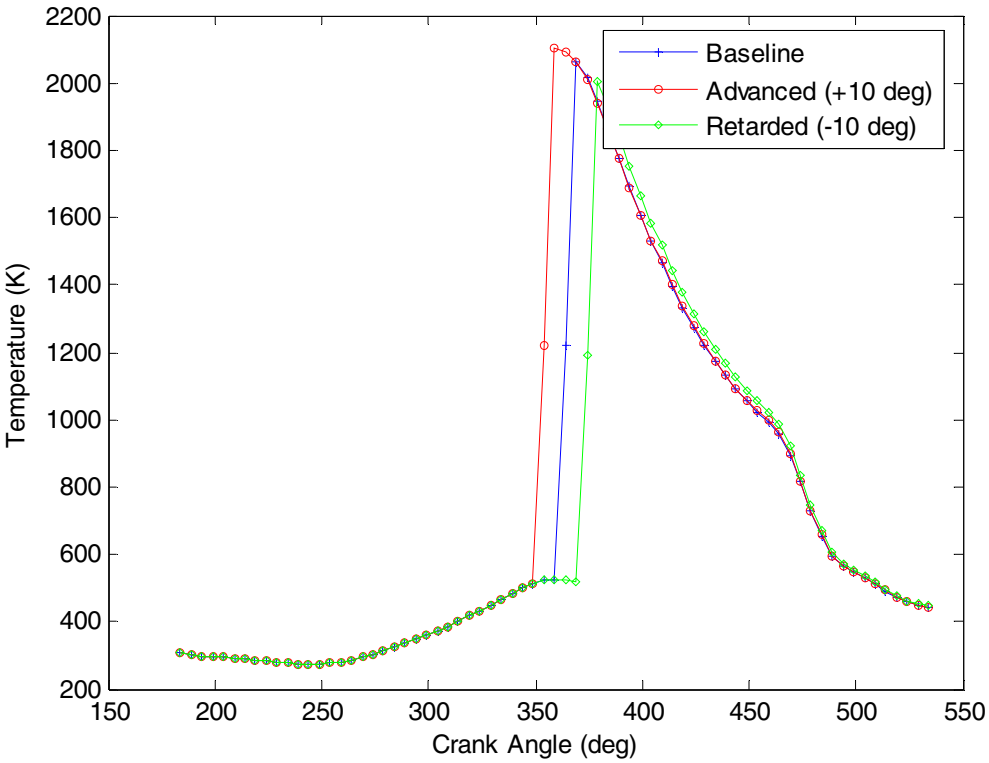

Figure 5.20: Effect of ignition timing on temperature

Figure 5.21 shows that the change in charge mass with respect to crank angle is not affected by the ignition timing. This makes sense because the charge mass should be mainly influenced by the port timing.

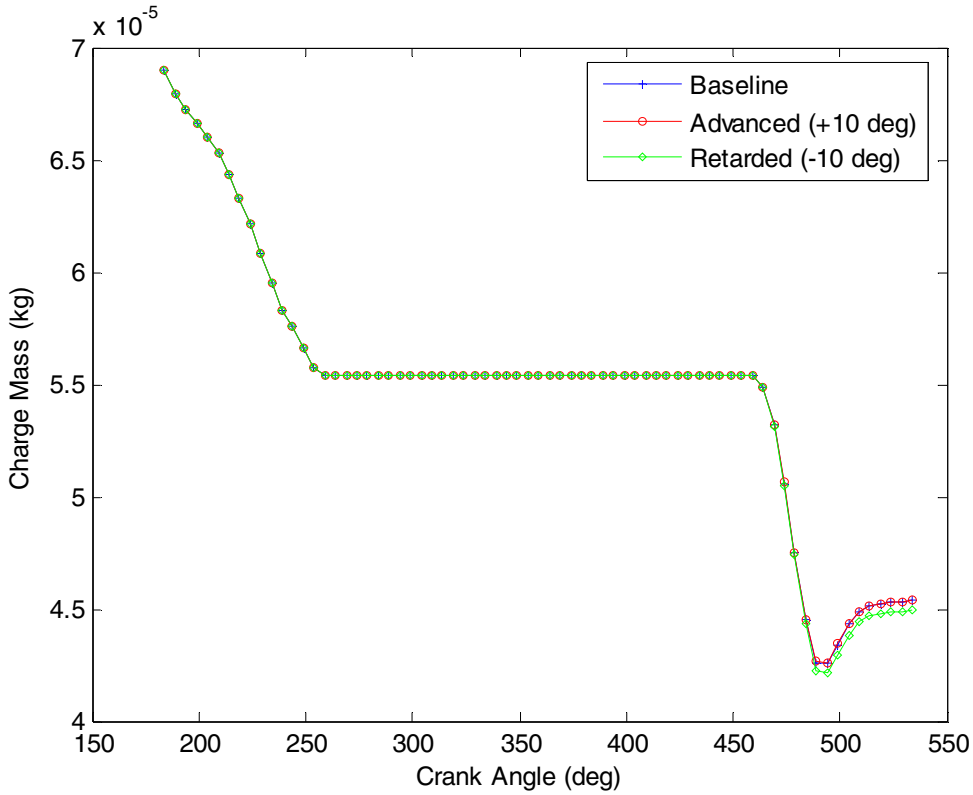

Figure 5.21: Effect of ignition timing on charge mass

Figure 5.22 shows PV diagrams for the different ignition timings. The area under each curve is integrated to find the indicated power. The results show that indicated power decreases with respect to the baseline value of 12.43 Hp for both cases. With the ignition advanced, the decrease in power was slight (-0.05 Hp). With the ignition retarded, the drop in power was somewhat larger (-0.47 Hp) but still close to the baseline indicated power. The results indicate that ignition timing appears to be near the optimal value and that engine performance is not extremely sensitive to it.

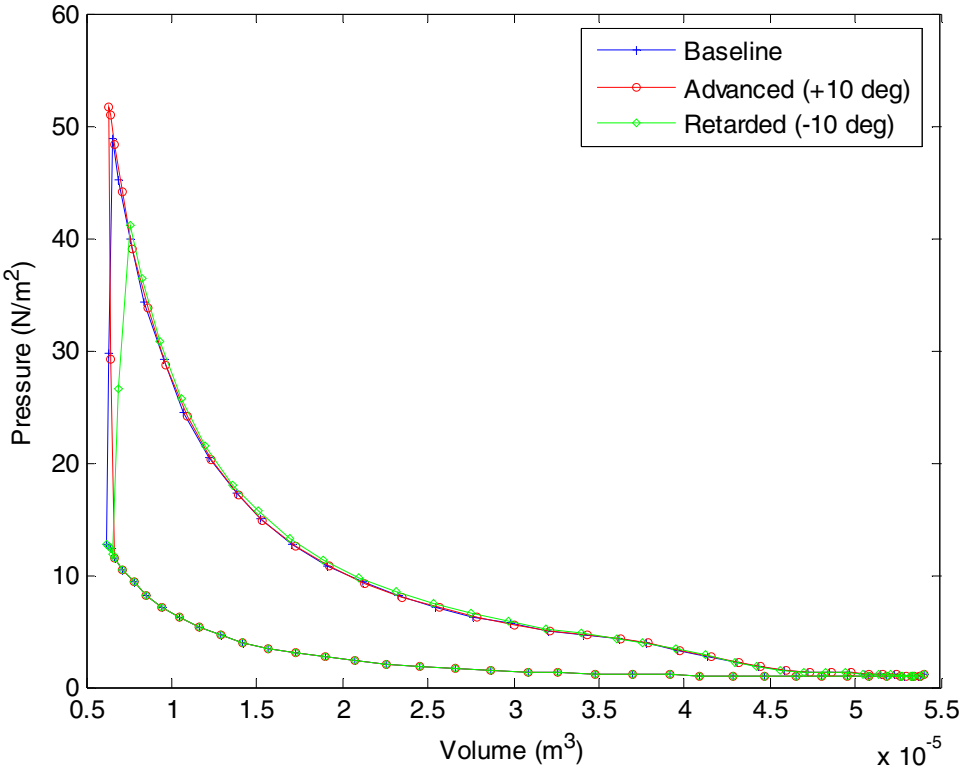

Figure 5.22: PV diagram for different ignition timing settings

Chapter 6: Conclusion

6.1 Experimental Measurement

A two-stroke gasoline engine presently powering a small, commercial UAV has been tested. Although it was not possible to acquire data for all possible combinations of operating speed and throttle position, the primary portion of the performance curve where the engine normally operates in was obtained. The maximum power output measured for the 3W 100i-B2 engine is 9.32 Hp at 8500 RPM and this value matches the manufacturer's claim for peak power within 0.2%. The overall efficiency of the engine is approximately 16% which is less than the 30% efficiency conventional-scale aero piston engines are able to achieve [39]. The reduced efficiency is in agreement with other experimental results obtained independently with smaller internal combustion engines [40]. The results also indicate that the dynamometer measurements are repeatable for separate runs and have an uncertainty for most test points of +/- 0.1 Hp and +/- 0.3% efficiency. The exhaust gas signature (HC, CO, CO_2, O_2) was characterized with an emissions analyzer and is consistent with the performance observations.

6.2 Computer Simulation

The engine was simulated using a MatLab code by specifying the engine dimensions and operating parameters. While the simulation did not correctly predict the actual performance of the engine, it did provide some insight into methods for

enhancing the performance of the engine. The simulation was scaled so that the power matched the indicated power calculated from the experimental testing, and the transfer port and exhaust port timing/duration and the ignition timing were varied in order to see what effect there was on engine performance. The simulation indicates that the engine is reasonably well optimized but that it might be possible to gain additional power (~ 1.5 Hp) by decreasing the exhaust port duration. This would shorten the exhaust blowdown phase on the power stroke and effectively capture more power from the expanding exhaust gases by keeping a higher pressure on the piston for a longer period of time. Decreasing the exhaust port duration would also shorten the amount of time the port is open on the compression stroke allowing for a higher pressure to build in the cylinder to generate increased power.

6.3 Future Work

Future testing on the engine in the short term could involve varying the air/fuel mixture to see what effect it has on performance. At present time it is unknown whether the air/fuel ratio, which is currently set at the manufacturer's recommended setting, is optimized for peak performance from the engine. Longer term work might incorporate replacing the engine's carburetor with a throttle body fuel injection system. The amount of fuel lost due to scavenging is unknown but as with similar 2-stroke engines of this size, the trapping efficiency is fairly poor. A throttle body would allow for more precise control over the amount of fuel being delivered to the cylinder and should result in increased efficiency. At ¼ and ½ throttle operation where the air/fuel ratio is rich in the higher RPM range, it should be possible to increase the efficiency from approximately 16% to nearly 20% by

allowing the engine to operate at a stoichiometric ratio and thus consuming less fuel. As shown in the following equation, the amount of fuel decreases by about 18% since the engine is running at stoichiometric:

$$\dot{m}_{f(stoich)} = \left(\frac{F/A_{stoich}}{F/A_{actual}} \right) \dot{m}_{f(actual)} = (0.82)\dot{m}_{f(actual)} \qquad \text{(Eq. 6.1)}$$

Where F/A_{stoich} equals 0.068 and F/A_{actual} is approximately 0.083 for ¼ and ½ throttle settings at speeds above 5500 RPM.

Future engine simulation work would concentrate on predicting the actual performance of the engine without having to scale the results to match the experimental data. Current limitations with the modeling used for heat release during combustion need to be corrected in order to obtain quantitative agreement with experimental data. If accurate performance values can be calculated, the simulation would prove to be very useful as a guide for understanding what might occur when testing or modifying new engines.

Bibliography

[1] http://www.nasm.si.edu/research/aero/aircraft/pioneer.htm, last downloaded 3/12/2007

[2] Bone, Elizabeth, Christopher Bolkcom, "Unmanned Aerial Vehicles: Background and Issues for Congress", Congressional Research Service, Library of Congress, 2003

[3] Jones, Christopher A., "Unmanned Aerial Vehicles (UAVs): An Assessment of Historical Operations and Future Possibilities", ACSC, March 1997

[4] Unmanned Aircraft Systems Roadmap 2005 - 2030, Office of the Secretary of Defense, August 2005

[5] Hill, Philip G., Carl R. Peterson, "Mechanics and Thermodynamics of Propulsion, Second Edition", United States, Addison Wesley Longman, 1992

[6] http://www.rotax-aircraft-engines.com/, last downloaded 6/29/2006

[7] Wohlwend, K. M., L. Q. Maurice, T. Edwards, "Thermal Stability of Energetic Hydrocarbon Fuels in Fuel Systems for Combined Cycle Engines", 35th AIAA/ASME/SAE/ASEE Joint Propulsion Conference and Exhibit, AIAA 99-2219, Los Angeles, California, 20-24 June 1999

[8] Wahla, N., D. Tither, W. Ahmed, D. Whitaker, "Preliminary Results from a Market Analysis of the Two-Stroke Combustion Engine Industry", Department of Chemistry, Manchester Metropolitan University, United Kingdom, 1997

[9] Singh, S., R. D. Reitz, M. P. B. Musculus, T. Lachaux, "Validation of Engine Combustion Models Against Detailed In-Cylinder Optical Diagnostics Data for a Heavy-Duty Compression-Ignition Engine", International Journal of Engine Research, 2007, Vol. 8

[10] Kurtz, E. M., D. E. Foster, "Identifying a Critical Time for Mixing in a Direct Injection Diesel Engine Through the Study of Increased In-Cylinder Mixing and its Effects on Emissions", International Journal of Engine Research, 2004, Vol. 5

[11] Tan, Zhichao, Rolf D. Reitz, "An Ignition and Combustion Model Based on the Level-Set Method for Spark Ignition Engine Multidimensional Modeling", Journal of Combustion and Flame, 2006, 1-15

[12] Lippert, A. M., D. W. Stanton, C. J. Rutland, W. L. Hallett, R. D. Reitz, "Multidimensional Simulation of Diesel Engine Cold Start with Advanced Physical Submodels", International Journal of Engine Research, 2000, Vol. 1

[13] http://www.erc.wisc.edu/, last downloaded 6/29/2006

[14] Davis, Gregory W., Adam E. Grobelny, John C. Stimpson, "Testing of a Conventional Two-Stroke Snowmobile Engine using Ethanol-Blended Fuels", Fourth International Energy Conversion Engineering Conference and Exhibit, AIAA 2006-4089, San Diego, California, 26-29 June 2006

[15] Aslam, M. U., H. H. Masjuki, M. A. Kalam, "An Experimental Investigation of CNG as an Alternative Fuel for a Retrofitted Gasoline Engine", Malaysia, September 2005

[16] Cadou, Christopher, Nathan Moulton, Shyam Menon, "Performance Measurement and Scaling in Small Internal Combustion Engines", 41st Aerospace Sciences Meeting and Exhibit, AIAA 2003-671, Reno, Nevada, 6-9 January 2003

[17] Menon, Shyam, Nathan Moulton, Christopher Cadou, "Development of a Dynamometer for Measuring Small Internal Combustion Engine Performance", Journal of Propulsion and Power, 2007, Vol. 23

[18] http://gram.eng.uci.edu/~ddunnran/, Portable Power Systems, last downloaded 3/21/2007

[19] Papac, Joseph, Derek Dunn-Rankin, "Characteristics of Combustion in a Miniature Four-Stroke Engine", Journal of Aeronautics, Astronautics and Aviation, 2006, Vol. 38

[20] Fu, Kelvin, Aaron J. Knobloch, Fabian C. Martinez, David C. Walther, Carlos Fernandez-Pello, Al P. Pisano, Dorian Liepmann, "Design and Fabrication of a Silicon-Based MEMS Rotary Engine", Proceedings of 2001 ASME International Mechanical Engineering Congress and Exposition, November 11-16, 2001, New York, NY

[21] Fernandez-Pello, A. Carlos, "Micro-Power Generation Using Combustion: Issues and Approaches", 29th International Symposium on Combustion, July 21-26, 2002, Sapporo, Japan

[22] http://www-bsac.eecs.berkeley.edu/groups/bmad/mems_reps/home.htm, last downloaded 3/21/2007

[23] Menon, Shyam, Christopher Cadou, "Experimental and Computational Investigations of Small Internal Combustion Engine Performance", 5th US Combustion Meeting, March 25-28, 2007, San Diego, California

[24] FA-50/30 SLV Eddy Current Dynamometer Owner's Manual, Borghi & Saveri.

[25] http://www.tokyometer.co.jp/, last downloaded 10/18/2006.

[26] Marcinkoski, Jason, “Baseline Engine Testing Report for Advanced Rotary Research”, 2004

[27] http://en.wikipedia.org/wiki/PID_control, last downloaded 10/19/2006

[28] http://www.3w-modellmotoren.com, last downloaded 10/19/2006

[29] 100iB2 Engine Owner’s Manual, 3W Modellmotoren

[30] http://www.ni.com/pdf/manuals/370721c.pdf, last downloaded 12/6/2006

[31] Industrial Deflection Gauge Owner’s Manual, Goodyear Eagle Pd

[32] Heywood, J.B., “Internal Combustion Engine Fundamentals”, New York, McGraw-Hill, 1988

[33] Ferguson, Colin R., Allan T. Kirkpatrick, “Internal Combustion Engines, Applied Thermosciences”, New York, John Wiley & Sons, Inc., 1986

[34] PXA-1100 Gas Analyzer Operator’s Manual, Vetronix Corporation, 1996

[35] SAE Standard, Engine Power Test Code-Spark Ignition and Compression Ignition-Net Power Rating, SAE J1349, Jun95

[36] http://wahiduddin.net/calc/density_altitude.htm, last downloaded 6/29/2006

[37] American Society of Mechanical Engineers, “Test Uncertainty”, ASME PTC 19.1-1998

[38] Turns, Stephen R., “An Introduction to Combustion: Concepts and Applications, Second Edition”, New York, McGraw-Hill, 2000

[39] http://www.answers.com/topic/internal-combustion-engine, last downloaded 3/19/2007

[40] Cadou, Christopher, Shyam Menon, “Scaling of Losses in Small IC Aero Engines With Engine Size”, 42nd Aerospace Sciences Meeting and Exhibit, AIAA 2004-690, Reno, Nevada, 5-8 January 2004